

Naval Research Laboratory

Washington, DC 20375-5000



2

NRL Memorandum Report 6799

AD-A233 717

Direct and Large-Eddy Simulations of Three-Dimensional Compressible Navier-Stokes Turbulence

T. A. ZANG,* R. B. DAHLBURG AND J. P. DAHLBURG

*Center for Computational Physics Developments
Laboratory for Computational Physics and Fluid Dynamics*

**Theoretical Flow Physics Branch
NASA Langley Research Center
Hampton, VA 23665*

April 2, 1991

ATC
APR 11 1991

AD-A233 717

Approved for public release; distribution unlimited.

97 4 10 11 12

REPORT DOCUMENTATION PAGE			Form Approved OMB No. 0704-0188	
Public reporting burden for this collection of information is estimated to average 1 hour per response, including the time for reviewing instructions, searching existing data sources, gathering and maintaining the data needed, and completing and reviewing the collection of information. Send comments regarding this burden estimate or any other aspect of this collection of information, including suggestions for reducing this burden, to Washington Headquarters Services, Directorate for Information Operations and Reports, 1215 Jefferson Davis Highway, Suite 1204, Arlington, VA 22202-4302, and to the Office of Management and Budget, Paperwork Reduction Project (0704-0188), Washington, DC 20503.				
1. AGENCY USE ONLY (Leave blank)	2. REPORT DATE 1991 April 2	3. REPORT TYPE AND DATES COVERED Interim		
4. TITLE AND SUBTITLE Direct and Large-Eddy Simulations of Three-Dimensional Compressible Navier-Stokes Turbulence			5. FUNDING NUMBERS PE - 611-53 TA - RR 011-09-43 - 1529	
6. AUTHOR(S) T. A. Zang, * R. B. Dahlburg, J. P. Dahlburg				
7. PERFORMING ORGANIZATION NAME(S) AND ADDRESS(ES) Naval Research Laboratory Washington, DC 20375-5000			8. PERFORMING ORGANIZATION REPORT NUMBER NRL Memorandum Report 6799	
9. SPONSORING/MONITORING AGENCY NAME(S) AND ADDRESS(ES) NASA Washington, DC 20546			10. SPONSORING/MONITORING AGENCY REPORT NUMBER ONR 800 N. Quincy St. Arlington, VA 22217-5999	
11. SUPPLEMENTARY NOTES *Theoretical Flow Physics Branch, NASA Langley Research Center, Hampton, VA 23665				
12a. DISTRIBUTION/AVAILABILITY STATEMENT Approved for public release; distribution unlimited.			12b. DISTRIBUTION CODE	
13. ABSTRACT (Maximum 200 words) This paper reports results from the numerical implementation and testing of the compressible large eddy-simulation [LES] model described by Speziale et al., (1988) and Erlebacher et al., (1990b). Relevant quantities from 32^3 "coarse grid" LES solutions are compared with results generated from direct numerical simulations [DNS] of three-dimensional compressible turbulence that have been run both with sufficient resolution, at 96^3 . We find that the 32^3 LES results overall agree well with their 96^3 DNS counterparts. Moreover, the new DNS results confirm several recent conclusions about compressible turbulence that have been based primarily on two-dimensional simulations.				
14. SUBJECT TERMS Large-Eddy Simulations Compressible turbulence Numerical methods			15. NUMBER OF PAGES 57	
			16. PRICE CODE	
17. SECURITY CLASSIFICATION OF REPORT UNCLASSIFIED	18. SECURITY CLASSIFICATION OF THIS PAGE UNCLASSIFIED	19. SECURITY CLASSIFICATION OF ABSTRACT UNCLASSIFIED	20. LIMITATION OF ABSTRACT SAR	

DIRECT AND LARGE-EDDY SIMULATIONS OF THREE-DIMENSIONAL COMPRESSIBLE NAVIER-STOKES TURBULENCE

1. Introduction

Recently, great effort has gone into accurate direct numerical simulation [DNS] of the compressible Navier-Stokes equations, both in 2-D (Passot and Pouquet, 1988; Grappin *et al* 1988; Gauthier, 1988; Sarkar *et al* 1989; Dahlburg *et al* 1990; Erlebacher *et al* 1990a) and in 3-D (Feiereisen *et al* 1981; Sarkar *et al* 1989; Erlebacher *et al* 1990b; Hossain and Mullan, 1990; Staroselsky *et al* 1990). These compressible simulations share with their incompressible DNS counterparts the restriction to relatively low Reynolds numbers that is required for adequate numerical resolution. For compressible flows, this low Reynolds number restriction is compounded by several additional factors: [1] at least one additional thermodynamic variable, *e.g.*, the mass density, must be retained and time-advanced, and this increases the required storage for the compressible problem; [2] as the Mach number increases, the average diagonal component of the Taylor microscale decreases (This decrease in one of the significant length scales, which is related to the tendency of acoustic waves to steepen, implies the requirement of more refined discretization as the Mach number increases (for the MHD analog *cf.* Dahlburg and Picone 1989)); and [3] the existence of cubic nonlinearities in the compressible equations makes the aliasing problem potentially more severe (*cf.* Canuto *et al* 1988).

The most interesting compressible flows for both pure research and for engineering purposes have much higher Reynolds numbers than those which currently can be simu-

lated accurately with DNS. Hence, some form of modeling is required in order to obtain sensible time-dependent results at the Reynolds numbers of interest. Several methods have been developed to address this Reynolds number problem for incompressible flows. These methods appear to generalize readily to the compressible case. For example, Pasot and Pouquet (1988) have investigated the use of hyperviscosities. Sakell (1988) has used second- and fourth-order artificial viscosities. Hossain and Mullan (1990) have used eddy viscosities in an astrophysical compressible convection problem. For the alternative Reynolds-averaging formulations see Speziale (1991).

We pursue here another approach, *viz.*, large-eddy simulation (LES) (*cf.* Moin and Kim 1982; Bardina *et al* 1983; Rogallo and Moin 1984; Piomelli *et al* 1989). We use the particular compressible large-eddy simulation (LES) formulation of Speziale *et al* (1988), hereafter *SEZHu*. An alternative compressible LES formulation has been furnished by Yoshizawa (1986).

We apply the computational techniques and simulation models outlined in *SEZHu* to the study of compressible turbulence. This research is directed toward implementation of a large-eddy simulation model capable of treating highly compressible, nearly inviscid turbulent flows. For clarity, we here study flows that are periodic in all three spatial directions. The long-range goal of this research is aimed at exploring the feasibility of using large-eddy simulations for computing components of flows in turbulent boundary layers around arbitrarily shaped vehicles at high speeds. At its present stage of sophistication LES also has constraints on the size of Reynolds numbers for which it is reliable. These constraints are more generous than those of DNS, but still fall short of what is required to simulate, say, a complete aircraft. Nevertheless, because it requires substantially less computer resources than DNS, LES does offer the hope of furnishing a reliable solution of a significant component of a full configuration (provided, of course, that suitable subgrid-scale models are available).

The structure of this paper is as follows. The governing equations, numerical algorithm, and initial conditions used in the simulations are outlined in the second section. In the third section we present the results of some new fully compressible DNS that supple-

ment the quasi-incompressible simulations provided by Erlebacher *et al* (1990b), and in the fourth section we discuss the results of LES for both quasi-incompressible and fully compressible cases. Finally, in the fifth section we enumerate our conclusions, and describe areas of further research.

2. Formulation of the problem

Simulation model:

Direct numerical simulations are performed of the compressible Navier-Stokes equations, written below in a familiar dimensionless form:

$$\frac{\partial \rho}{\partial t} + \nabla \cdot (\rho \mathbf{v}) = 0, \quad (1)$$

$$\frac{\partial \rho \mathbf{v}}{\partial t} + \nabla \cdot (\rho \mathbf{v} \mathbf{v}) = -\nabla p + \frac{1}{Re} \nabla \cdot \sigma, \quad (2)$$

$$\frac{\partial p}{\partial t} + \mathbf{v} \cdot \nabla p + \gamma p \nabla \cdot \mathbf{v} = \frac{(\gamma - 1)}{Re} \Phi + \frac{1}{M_\infty^2 Pr Re} \nabla \cdot (\mu \nabla T), \quad (3)$$

where the viscous stress tensor σ_{kl} is given by:

$$\sigma_{kl} = -\frac{2}{3} \mu (\nabla \cdot \mathbf{v}) \delta_{kl} + \mu \left(\frac{\partial v_k}{\partial x_l} + \frac{\partial v_l}{\partial x_k} \right),$$

and the viscous dissipation Φ is given by:

$$\Phi = \sigma_{kl} \frac{\partial v_k}{\partial x_l} = -\frac{2}{3} \mu (\nabla \cdot \mathbf{v})^2 \delta_{kl} + \mu \left(\frac{\partial v_k}{\partial x_l} + \frac{\partial v_l}{\partial x_k} \right) \frac{\partial v_k}{\partial x_l}.$$

The system is closed with an equation of state:

$$\gamma M_\infty^2 p = \rho T. \quad (4)$$

In the above equations the symbols have the following meanings: $\rho \equiv$ mass density; $\mathbf{v} = (u, v, w) \equiv$ velocity; $p \equiv$ thermal pressure; $T \equiv$ temperature; $\mu \equiv$ viscosity; $\gamma = 1.4 \equiv$ adiabatic index for air; $M_\infty \equiv$ free-stream Mach number; $Pr = .72 \equiv$ Prandtl number; and

$Re \equiv$ Reynolds number. The density, velocity, temperature and viscosity were scaled by reference values, with the pressure scaled by the product of the reference density and the square of the reference velocity. The Reynolds number is based on the reference values of the velocity, length, viscosity and density. For the isotropic turbulence problem of specific interest in this paper the flow was assumed to be periodic with period 2π in each coordinate direction and the viscosity was presumed to be a constant.

We have assembled and tested a computer simulation code which can perform compressible large-eddy or direct numerical simulations of equations (1) - (4). The LES model used in this code is based on the *SEZHu* subgrid-scale model, relevant elements of which we now review.

In the subgrid-scale model, flow variables F are first spatially filtered,

$$\bar{F}(\mathbf{x}) = \int_0^{2\pi} \int_0^{2\pi} \int_0^{2\pi} G(\mathbf{x} - \mathbf{z}, \Delta) F(\mathbf{z}) d^3 z,$$

where G is the filter function (taken to be a Gaussian plus a cutoff filter in the present work), and Δ is the filter width. The turbulent fields F are then assumed to be decomposed in the following way:

$$F = \tilde{F} + F', \quad (5)$$

in which the Favre filter is defined by:

$$\tilde{F} = \frac{\overline{\rho F}}{\bar{\rho}}. \quad (6)$$

Using these definitions, the dimensionless, filtered, partial differential equations which are used in the large-eddy simulation code are the continuity equation:

$$\frac{\partial \bar{\rho}}{\partial t} + \nabla \cdot (\bar{\rho} \bar{\mathbf{v}}) = 0, \quad (7)$$

the vector momentum equation:

$$\frac{\partial \bar{\rho} \tilde{\mathbf{v}}}{\partial t} + \nabla \cdot (\bar{\rho} \tilde{\mathbf{v}} \tilde{\mathbf{v}}) = -\nabla \bar{p} + \frac{1}{Re} \nabla \cdot \bar{\boldsymbol{\sigma}} + \nabla \cdot \boldsymbol{\tau}, \quad (8)$$

and the thermal pressure equation:

$$\begin{aligned} \frac{\partial \bar{p}}{\partial t} + \tilde{\mathbf{v}} \cdot \nabla \bar{p} + \gamma \bar{p} \nabla \cdot \tilde{\mathbf{v}} &= (\gamma - 1) \overline{\mathbf{v} \cdot \nabla p} - (\gamma - 1) \tilde{\mathbf{v}} \cdot \nabla \bar{p} + \\ & \frac{(\gamma - 1)}{Re} \bar{\Phi} + \frac{1}{M_\infty^2 Pr Re} \nabla \cdot (\kappa \nabla T) + \frac{1}{M_\infty^2} \nabla \cdot (-\mathbf{Q}) \end{aligned} \quad (9)$$

In Eq. (8) the subgrid-scale stress tensor is given by

$$\tau_{kl} = -\bar{\rho} (\widetilde{\tilde{v}_k \tilde{v}_l} - \tilde{v}_k \tilde{v}_l + \widetilde{v'_k \tilde{v}_l} + \widetilde{\tilde{v}_k v'_l} + \widetilde{v'_k v'_l}),$$

and the subgrid-scale heat flux in Eq. (9) is:

$$Q_k = -c_p \bar{\rho} (\widetilde{\tilde{v}_k \tilde{T}} - \tilde{v}_k \tilde{T} + \widetilde{v'_k \tilde{T}} + \widetilde{\tilde{v}_k T'} + \widetilde{v'_k T'}),$$

where $c_p \equiv$ specific heat at constant pressure. The equation of state becomes:

$$\gamma M_\infty^2 \bar{p} = \bar{\rho} \tilde{T}. \quad (10)$$

Following the *SEZHu* approach, we model the subgrid-scale (SGS) stress as:

$$\tau_{kl} = -\bar{\rho} (\widetilde{\tilde{v}_k \tilde{v}_l} - \tilde{v}_k \tilde{v}_l) + 2 C_R \bar{\rho} \Delta^2 \Pi_{\tilde{S}}^{\frac{1}{2}} (\tilde{S}_{kl} - \frac{1}{3} \tilde{S}_{mm} \delta_{kl}) - \frac{2}{3} C_I \bar{\rho} \Delta^2 \Pi_{\tilde{S}} \delta_{kl}, \quad (11)$$

where $\delta_{kl} \equiv$ Kronecker delta. The Favre filtered rate-of-strain tensor, \tilde{S}_{kl} , is given by:

$$\tilde{S}_{kl} = \frac{1}{2} \left(\frac{\partial \tilde{v}_k}{\partial x_l} + \frac{\partial \tilde{v}_l}{\partial x_k} \right),$$

and its second invariant is:

$$\Pi_{\tilde{S}} = \tilde{S}_{mn} \tilde{S}_{mn}.$$

The SGS heat flux is modelled as:

$$Q_k = c_p \bar{\rho} \left[(\widetilde{\tilde{v}_k \tilde{T}} - \tilde{v}_k \tilde{T}) - C_T \Delta^2 \Pi_{\tilde{S}}^{\frac{1}{2}} \frac{\partial \tilde{T}}{\partial x_k} \right]. \quad (12)$$

In both Eqs. (11) and (12) the first right-hand-side terms are the scale-similarity portion of the model and the remaining part of the right-hand-side is the Smagorinsky portion. (What we refer to here as the scale-similarity portion of the model is the model for the *sum* of the Leonard and cross stresses.)

The constants in the above equations; Δ , C_R , C_I , and C_T , must be specified in order to close the model. The values recommended by *SEZHu*, obtained by analysis of quasi-incompressible DNS, are:

$$\Delta = 2(\Delta x), \quad (13)$$

$$C_R = 0.012, \quad (14)$$

$$C_I = 0.0066, \quad (15)$$

where Δx is the grid spacing for the grid used in the LES. We use these values to define the standard case for the computations reported in this paper. The dimensionless constant, C_T , can be expressed in terms of C_R and a turbulent Prandtl number, Pr_T :

$$C_T = \frac{1}{Pr_T} C_R = 0.017 \quad (16)$$

where we have used the conventional value of $Pr_T = 0.7$ instead of the value of 0.4 reported by *SEZHu*. The latter value of Pr_T was based on analysis of a quasi-incompressible set of DNS, and may not be general enough to apply to strongly compressible systems.

Strictly speaking, the *SEZHu* SGS model requires de-filtering (and subsequent re-filtering) for the computation of the molecular viscous term in Eq. (8) and for the first, third, and fourth terms on the right-hand side of Eq. (9). For the present LES we simplify the computations (and avoid the potentially unstable de-filtering procedure) by simply [a] using $\tilde{\sigma}$ rather than $\bar{\sigma}$ in Eq. (8), [b] setting the sum of the first and second right-hand side terms of Eq. (9) to zero, [c] using $\Phi(\tilde{\mathbf{v}})$ instead of $\bar{\Phi}$, and [d] treating the molecular conductivity term in Eq. (9) in a manner similar to the treatment of the viscous term in Eq. (8).

In the DNS code, the spatial discretization is Fourier collocation in x, y and z , with evenly spaced collocation points. A time-step splitting technique is employed which allows

the sound waves to be integrated exactly in time (Erlebacher *et al* 1990b). The other terms are advanced using a third-order, low-storage Runge-Kutta explicit time-stepping scheme. At the end of each stage isotropic truncation is applied to ensure that only those modes with $k_x^2 + k_y^2 + k_z^2 \leq (N/2)^2$ are non-zero. The semi-implicit scheme enables the use of time steps on the order of a CFL restriction in which the sound speed is neglected, a feature which becomes increasingly valuable at lower Mach numbers.

With this algorithm, a 32^3 large-eddy simulation requires approximately 1.2 million words of core memory, and approximately 2.7 seconds per time step on the NAS Cray Y-MP. A 32^3 direct simulation with the same code requires only 1.3 seconds per step. But the more relevant timing comparison is to that of the DNS code running on a 96^3 grid, which takes 30 sec/step and requires roughly 3 times as many steps per unit time as the LES computation.

In-line diagnostics include but are not limited to: [1] global quantities such as energies (solenoidal, irrotational, kinetic and internal); viscous dissipation; *RMS* Mach number; variances of significant fields; maxima and minima of significant fields; [2] spectra of many quantities (*e.g.* velocity; mass density; temperature; thermal pressure; kinetic energy; enstrophy; compressible and solenoidal kinetic energies) and; [3] various meaningful *RMS* quantities at the tensor level (for example, Taylor microscales and velocity derivative skewness and flatness).

3. DNS Data base

The DNS that *SEZHu* used in their preliminary study of the compressible subgrid-scale model covered a limited parameter range. In fact, because not only the initial divergence but also the initial time derivative of the divergence were set to zero (following the work of Feiereisen *et al* 1981), the compressible component of the flow remained quite small throughout the simulations. In the present work we have supplemented those quasi-incompressible simulations with fully compressible ones, and also continued the former simulations to much later times. The precise choice of parameters for the new DNS was strongly influenced by the work of Erlebacher *et al* (1990a) and Sarkar *et al* (1989), who have clarified the effect of initial conditions for compressible turbulence.

For compressible turbulence it is important to distinguish the the solenoidal component of the velocity field, denoted by \mathbf{v}^s , from the irrotational component, denoted by \mathbf{v}^c . (We shall also refer to these two components as the incompressible and compressible components, respectively.) The Helmholtz decomposition is unique for the case of isotropic turbulence, and in Fourier space it is given by

$$\hat{\mathbf{v}}^c = \frac{\mathbf{k} \cdot \hat{\mathbf{v}}}{k^2} \mathbf{k}, \quad (17)$$

and

$$\hat{\mathbf{v}}^s = \hat{\mathbf{v}} - \hat{\mathbf{v}}^c, \quad (18)$$

where $\hat{\mathbf{v}}$ is the Fourier transform of the velocity, and \mathbf{k} is the Fourier wavenumber. Now consider the integral over the computational domain of the kinetic energy per unit mass,

$$E = \frac{1}{2} \int_0^{2\pi} \int_0^{2\pi} \int_0^{2\pi} |\mathbf{v}|^2 dx dy dz; \quad (19)$$

we shall refer to this quantity hereafter (somewhat imprecisely) as just the kinetic energy. Let E^s and E^c denote the contributions to this integral from the solenoidal and irrotational velocity components. Let $\chi = E^c/E$ denote the ratio of compressible kinetic energy to the total kinetic energy, and let p_c denote the ratio of the *RMS* pressure fluctuation to the mean pressure. As shown by Sarkar *et al* (1989), the turbulence should, on the acoustic time scale, approach asymptotically a state in which the non-dimensional parameter $F = \gamma M^2 \chi / p_c^2$ reaches unity. Here M , termed the turbulent Mach number, is the average Mach number of the velocity fluctuations. The present fully compressible initial conditions were chosen to cover a range of M and χ , with the initial pressure fluctuations chosen so that the initial value of F was unity. This choice avoids the boundary layer in time that would otherwise be present for a more arbitrary, but probably less physically realistic, choice of initial conditions (Erlebacher *et al* 1990a).

Table I summarizes the complete set of DNS that was used in the present work. The initial energy spectra for the old quasi-incompressible runs (those denoted by QIC) were chosen by Erlebacher *et al* (1990b) to match the experimental spectra of Comte-Bellot and Corrsin (1962), whereas the initial energy spectra for the new runs (denoted by MC)

had the form $E(k) = k^4 \exp(-k^2/2k_0^2)$, with the RMS velocity fluctuation set to unity. In the new runs the initial density fluctuations were zero, implying that all of the pressure fluctuations arose from temperature fluctuations. (This choice was made to simplify the enforcement of zero net linear momentum in the initial conditions.) The initial molecular Reynolds number for the MC cases was 250, corresponding to an initial Taylor microscale Reynolds number of approximately 27 for all but the M01C02K5 case, for which it was 53. The table contains the initial values of E/ϵ , where ϵ is the total dissipation. This quantity is a measure of the large-eddy turnover time.

A comparison of the initial energy spectra, $E(k)$, is presented in Figure 1 for the cases QIC01, M01C02, and M01C02K5. The initial spectra for all the QIC cases were the same, and the initial spectra for all the new cases except the last two were the same as for the M01C02 case (aside from the relative proportions of the incompressible and compressible components). The energy spectra for the two QIC cases had their peaks at $k = 1$ and decayed relatively slowly for large k , whereas the MC cases had their peaks at larger k and decayed relatively rapidly. Figure 1 also contains the spectra at a later stage for each of these three cases. In all three examples shown in the figure the spectra at the later stage exhibited a decay of more than three orders of magnitude from the peak to the tail, and the curl at the tail was quite mild. This indicates that the turbulent flows were resolved adequately. The value chosen for the molecular viscosity for the new DNS runs was determined by the criterion that a 96^3 simulation be well-resolved and that even a 64^3 simulation be inadequate.

Figures 2 and 3 furnish the time evolution of the key diagnostics of the QIC runs. (The results for these earlier runs are presented here in different units from those used by Erlebacher *et al* 1990b. The velocities have been divided by $6.75 \sqrt{3}$ and the time has been multiplied by the same factor. This has been done so that the initial RMS velocity fluctuation was unity, matching that of the new DNS runs. They also have been run about an order of magnitude longer in time.) In the quasi-incompressible case QIC01 the flow first settles into a quasi-equilibrium state with the parameter F holding relatively constant at the small value of 0.007. This state lasts until roughly $t = 3$, at which time the flow transitions rapidly into a new, quasi-equilibrium state with $F \approx 1$. The calculations for

this case reported by Speziale *et al* (1988) and Erlebacher *et al* (1990b) were conducted only until $t = 1.34$, which was before the transition. By $t = 4$ the resolution of the 96^3 DNS became inadequate due to strong activity at small scales in the irrotational component. The QIC04 results, shown in Figure 3, exhibit a more gradual approach to the expected asymptotic state. Note that the initial conditions for the QIC01 and QIC04 simulations did not meet the assumptions of the theory developed by Erlebacher *et al* (1990a) and applied by Sarkar *et al* (1989) to predict the asymptotic state (Erlebacher 1990, private communication). A more refined theory is required to explain the details of these two simulations. This difference in the time scale for the transition is related to the difference in the characteristic acoustic periods for the two cases. This issue is addressed below.

Figures 4 - 12 give the time evolution of the same key diagnostics for the MC runs. Note that the compressible component for the new quasi-compressible case, M01C00, remains negligible throughout that simulation. Nevertheless, as a function of time the non-dimensional parameter F does approach unity for the M01C00 simulation. For all the remaining new simulations the parameter F remains quite close to one, although typically the fluctuations of F have increasing amplitude and longer period as time increases. These fluctuations occur on the acoustic scale and their period is approximately $\tau = 2\pi/k_p \bar{c}$, where k_p is the wavenumber for the peak in $E(k)$ and \bar{c} is the average sound speed (equal to $1/M$ for these cases). Initially, $k_p \approx k_0$ and $\tau \approx 0.6M$ for the $k_0 = 10$ cases and $\tau \approx 0.12$ for the $k_0 = 5$ cases. The initial time scale of the fluctuations in F in Figures 4-12 conform to these estimates. The increase with time of the period of the fluctuations in F corresponds to the shift in the energy spectra towards smaller wavenumbers caused by the more rapid decay of the smaller scale velocity components - see Figure 1.)

Let us now reconsider the rate of approach to the asymptotic state for the three quasi-incompressible runs. The acoustic periods for the cases QIC01, QIC04 and M01C00 are approximately 0.06, 0.6, and 2.5, respectively (using $k_p = 1$ for the QIC runs and $k_p = 10$ for M01C00). The rate of approach to the asymptotic state, and the time scale of the fluctuations in F for the QIC04 and M01C00 cases are consistent with estimates based on the initial acoustic period. The transition to the asymptotic state for the QIC01 case and the time scale of the fluctuations are both much faster than this estimate. The reason

for this is unclear, but it is probably related to the presence of a substantial irrotational component of dissipation in the QIC01 example. It is unlikely to be due to shocks in the QIC01 simulation. Figure 13 displays some additional diagnostics for this case. Since the extrema of the divergence of velocity are quite symmetrical, the work of Erlebacher *et al* (1990a) allows us to conclude that shocks are not present.

The tendency of F to remain close to unity in the MC DNS provides corroboration in 3-D of the 2-D results of Sarkar *et al* (1989). The parameter χ typically evolves slowly, on what appears to be the viscous time scale. It increases slightly for those cases with an initial χ less than 0.5 and decreases slightly for the remaining cases.

The kinetic energy E decays monotonically for all cases. Although the total dissipation ϵ also decays monotonically for the QIC simulations, for the MC ones it increases initially and then decays. The dissipation is composed of solenoidal and irrotational components, *viz.*, $\epsilon = \epsilon^s + \epsilon^c$, where

$$\epsilon^s = \int_0^{2\pi} \int_0^{2\pi} \int_0^{2\pi} |\nabla \times \mathbf{v}|^2 dx dy dz, \quad (20)$$

and

$$\epsilon^c = \frac{4}{3} \int_0^{2\pi} \int_0^{2\pi} \int_0^{2\pi} |\nabla \cdot \mathbf{v}|^2 dx dy dz. \quad (21)$$

The initial total dissipation increases with χ , by an amount precisely attributable to the factor of 4/3 in ϵ^c .

The peak in the total dissipation for the MC simulations is of some interest. It occurs at $t_e \approx 0.1Re/k_0^2$, although as χ increases, t_e decreases slightly. For small M and χ this peak is concentrated in the solenoidal component. However, as M or χ increases, the peak shifts increasingly to the irrotational component. The recent mathematical analysis of incompressible, isotropic turbulence by Henshaw *et al* (1989) suggests a possible explanation for this phenomenon. They have described this initial phase (until shortly after t_e) as the maximally dissipative phase. It is characterized by a relatively slow decay of the spectrum as a function of k . The flow then evolves into a less dissipative state, with large coherent structures and a more rapid decrease of the spectrum as a function of k . Indeed, an analysis of the spectra of the present simulations indicates that $E^c(k)$ decays

more slowly as the peak in the dissipation shifts toward ϵ^c . The QIC cases evidently were begun closer to a maximally dissipative state than the MC cases due to the much slower decay of their initial spectra.

The fluctuations in the thermodynamic variables, ρ , p and T , achieve quasi-equilibrium after a few acoustic periods. Note that the density fluctuations, although initially zero, end up larger than the temperature fluctuations. In all of the $k_0 = 10$ cases the initial transient phase has concluded by $t = 0.4$ — the dissipation has peaked and the thermodynamic fluctuations have settled down to their asymptotic proportions.

Figure 14 displays some additional diagnostics for the case M01C02. (Although this case is occasionally singled out in this paper for special attention, similar behavior is exhibited by the other new cases.) The curves for the extrema of the velocity divergence are virtually anti-symmetric, which, as stated before, is indicative of compressible turbulence in which shocks are absent (Erlebacher *et al* 1990a; Picone and Dahlburg, 1991). The pressure dilatation term, $p'\nabla \cdot \mathbf{v}$, is strongly oscillatory but its average value is much smaller than the compressible dissipation. This provides further support for the neglect of the pressure dilatation term employed by Sarkar and Balakrishnan (1990) in their proposed Reynolds stress model for compressible turbulence. The skewness and flatness both reach quasi-equilibrium by $t = 0.4$. The corresponding plots for the remaining new cases reveal that as M or χ increase the skewness becomes more negative and the flatness more positive.

Figure 15 displays the energy spectra at various early times for the case M01C02. The energy spectra have the slowest decay (as a function of k) near the time of maximal dissipation (roughly at $t = 0.25$), and at later times they decay as a function of k at a faster rate (see Figure 1).

4. Large-eddy simulations

Quasi-incompressible results:

As our first test of the LES model we use the direct numerical simulations described by *SEZHu*, which are the two QIC cases in Table I, together with the case M01C00, which is a new quasi-incompressible case with a vastly different initial energy spectrum.

The QIC data generated by *SEZHu* at 96^3 have been stored at six equally spaced times, including the initial conditions. For purposes of comparing the 96^3 DNS results with the LES, we apply a 32^3 cutoff filter to this data (to project it onto the 32^3 grid), and then apply the same Gaussian filter that is used in the LES runs. The filtered 96^3 data at $t = 0$ serves as the initial conditions for the 32^3 LES run, with all other parameters such as Reynolds and Mach numbers remaining the same. Therefore, the comparison of the LES and DNS results is presented for the *resolved* (or large-scale) fields. To close the SGS model, we use for now the coefficients C_R and C_I given by *SEZHu*, but set C_T to correspond to $Pr_T = 0.7$ (see Eqs. (13)-(16)). At subsequent intervals, we compare the filtered 96^3 data with the 32^3 LES results.

The LES results for the two QIC cases are shown in Figures 16 and 17 and they are compared there with the fine-grid DNS results. In these two cases the resolved field contained 66% of the total kinetic energy, or, in other words, the subgrid-scale energy comprised 34% of the kinetic energy. (*SEZHu* also presented quasi-incompressible results for a fluctuating Mach number of 0.6. This case happens to be perilously close to the upper limit of fluctuating Mach number for this particular energy spectrum: at values of M much larger than 0.6 the 96^3 DNS breaks down because the fluctuations are so large that they produce negative temperatures. The LES for the QIC06 case has similar problems and therefore no results are presented for it.)

The compressible kinetic energy comprises less than 0.1% of the total kinetic energy, as expected for these quasi-incompressible cases. The *SEZHu* model produces quite good predictions for the evolution of the incompressible kinetic energy and for the density and temperature fluctuations. The predictions for the compressible kinetic energy are less accurate. The errors for it, however, are not particularly bothersome since it makes an inconsequential contribution to the total kinetic energy in these quasi-incompressible cases.

Figure 18 provides a similar comparison for the additional, new quasi-incompressible case M01C00. The coarse-grid LES was begun at $t = 0.4$, a time which is beyond the peak in the dissipation and after the turbulence statistics have settled down. Here we find even better agreement between the coarse-grid LES results and those of the fine-grid DNS

for the solenoidal kinetic energy. This is especially encouraging, considering that for this example, the resolved portion of the kinetic energy is only 35% of the total. The errors in the LES predictions for the compressible kinetic energy and the temperature and density fluctuations are somewhat larger. However, all three of these quantities are rather small and these errors have very little effect on the rate of decay of the turbulence.

We thus are satisfied that the model performs adequately in the quasi-incompressible regime. However, it is clear that the model must be tested on flows which are highly compressible. We now turn to a discussion of results from simulations with an appreciable compressible kinetic energy component.

Strongly compressible results:

As in the previous section, two simulations are presented for each case selected: a 96^3 DNS and a 32^3 LES. We begin with the application of the *SEZHu* model with the standard parameters for most of the compressible ($\chi > 0$) MC cases listed in Table I. The results are given in Figures 19-24. The LES perform quite well, especially considering the large fraction of kinetic energy which resided in the subgrid scales – 65% for the $k_0 = 10$ cases and 32% for the $k_0 = 5$ case. Indeed, the LES predictions for the solenoidal kinetic energy and the temperature fluctuations are comparable in accuracy to those for the earlier quasi-incompressible cases, whereas the predictions for the now non-negligible compressible kinetic energy and the density fluctuations are typically better.

These data allow us to draw some general conclusions about the performance of the *SEZHu* model as a function of the parameters M and χ . [1] The SGS model is slightly too dissipative for E^s , and this error decreases with increasing M but increases with increasing χ . [2] The SGS model is too dissipative for E^c , and this error decreases with M and decreases with χ . [3] The most important conclusion, however, is that the *SEZHu* subgrid-scale model produces LES results that make predictions for the temporal decay of the total kinetic energy decay that are just as good for strongly compressible flow as for incompressible flow. Indeed, in some respects, the model performs better for the strongly compressible cases than for the quasi-incompressible ones.

Next, we consider variations in the SGS model, focusing on the case M01C02. The series of LES runs we have performed for this case are summarized in Table II. The run labelled M01C02a in Table II, the LES case with the standard coefficients, is shown in Figure 19 along with results of runs for which only the generalized Smagorinsky portion (case M01C02b) or only the scale-similarity portion (case M01C02c) are active. A similar comparison for the case M01C06 is furnished in Figure 21. Clearly, most of the SGS dissipation is furnished by the Smagorinsky component, although some SGS dissipation is produced by the scale-similarity contribution.

The following series of LES focus on the effects of the Smagorinsky coefficients, C_R , C_I , and C_T . In these and subsequent LES we retain the scale-similarity component. Figure 25 displays the effects of changing the value of the Smagorinsky constants up or down by 10% from the values recommended by *SEZHu* on the basis of *a priori* tests for a quasi-incompressible DNS data base (cases M01C02a, M01C02d, and M01C02e). Reducing the values by 10% produces near perfect agreement for the decay of the solenoidal kinetic energy but still leaves a substantial error in the compressible kinetic energy.

We consider now the contribution arising from that component of the *SEZHu* model – the one with the coefficient C_I – which might be expected to contain strong compressibility effects. The relevant cases here are M01C02a, M01C02f, M01C02m, and M01C02n. These cover a range of C_I from 0 to 50 times the standard value of 0.0066. The results are summarized in Figure 26. The graphs for the cases with $C_I = 0$, $C_I = 0.0066$ and $C_I = 0.066$ are virtually indistinguishable. (We haven't even bothered to plot the first of these in the figure.) A 50-fold increase in C_I , however, produces a marked reduction in the decay of E^c (and also slows the decay of the pressure and temperature fluctuations), while having little effect upon E^s .

The effect of the turbulent Prandtl number is illustrated in Figure 27. The basis of comparison is run M01C02e, in which C_R has been tuned to give the best predictions of E^s and for which C_I has an inconsequential effect on the LES results. In the comparison runs $C_I = 0$, $C_R = 0.0108$ and Pr_T is half (case M01C02j) and 1.5 times (case M01C02k) its nominal value of 0.70, respectively. We observe that Pr_T has little effect upon E^s , whereas

decreasing it has a favorable effect upon E^c , and an adverse effect upon the temperature fluctuations. Increasing Pr_T has the reverse effects.

Finally, we illustrate the effect of filter width upon the results. All of the LES reported above used a filter width of twice the grid size on the coarse, 32^3 grid. Figures 28 and 29 show the results for LES using the *SEZHu* model, but with filter widths of one and four times the grid size. (cases M01C02h and M01C02i, respectively). As expected, the relative errors increase with the filter width.

To summarize what this series of tests has revealed about the influence of the various components of the *SEZHu* compressible SGS model: [1] The generalized Smagorinsky component produces most, but not all, of the SGS dissipation. [2] As C_I is increased the dissipation of the compressible component is decreased, while the solenoidal component is barely affected. [3] As C_T is decreased the dissipation of the compressible component is decreased, while the solenoidal component is barely affected. [4] The principal Smagorinsky constant, C_R , should be reduced by about 10% from its recommended value.

The preceding *a posteriori* tests of the SGS model indicate that better agreement can be obtained for LES of the case M01C02 by choosing $C_R = 0.0108$, $C_I = 0.33$, and $C_T = 0.0231$ (case M01C02p). The results of such a LES with these revised constants are given in Figure 30. The results using these constants are excellent for all the significant flow variables. We have included in Figure 30 a comparison with a coarse-grid, 32^3 DNS run. This was done to indicate the effect of the SGS model. The coarse-grid DNS makes predictions which are much poorer than those obtained with the SGS model.

Within the context of the *SEZHu* model, however, these optimal constants are far from universal over the range of M and χ . Figures 31 and 32 display the results of LES with these revised constants for the cases M01C06 and M03C02, respectively. These results are consistent with our earlier observations on how the errors in the kinetic energy components vary with M and χ . The success in tuning the model constants for the M01C02 case indicates that including an empirical dependence of C_R , C_I , and C_T upon M and χ might lead to more universally acceptable predictions of the large-eddy simulations. A more preferable alternative, however, would be to modify the *SEZHu* model itself so that it produces acceptable predictions without *ad hoc* modifications to the "constants".

5. Conclusions

The direct numerical simulations reported in Section 3 for the most part conformed to the recently developed theory of compressible turbulence by Erlebacher *et al* (1990a). However, the extended calculation of the $M = 0.1$ QIC case did reveal one feature, namely, the rapid transition to the asymptotic state, that is currently unexplained. An interesting feature of the MC cases was shift in the peak in the dissipation from the incompressible to the compressible component as the level of compressibility increased.

The results from the large-eddy simulations of compressible turbulence are encouraging. Even with the originally recommended coefficients for the *SEZHu* model the predictions are rather good for the evolution of such compressible quantities as the compressible component of kinetic energy and the fluctuations in the thermodynamic variables. Although the LES predictions can be improved for particular cases by changes in the model constants, the appropriate changes are apparently a function of compressibility (M and χ). A more complete set of LES could presumably furnish enough data to suggest an empirical dependence of these "constants" on the compressibility parameters. The development of a revised subgrid-scale model that required no explicit adjustment of the constants with compressibility would be preferable.

Compressible LES technology has been tested in this paper for only the simplest case. It should also be verified for isotropic turbulence containing shocks, and then it should be extended to such canonical flows as homogeneous, uniform shear flow. Ultimately, it must be demonstrated for inhomogeneous, wall-bounded flows and for complex geometries.

Acknowledgements:

We are pleased to acknowledge helpful discussions with Gordon Erlebacher, Yousuff Hussaini, Ugo Piomelli, Charles Speziale, Sutanu Sarkar, and J. H. Gardner. Financial support for RBD and JPD was provided by DARPA. RBD was also supported by the NASA Space Physics Theory Program. The numerical simulations were performed on the NASA-ARC Cray Y-MP under the Numerical Aerodynamic Simulation Program and on the NASA-LRC Cray-2.

REFERENCES

- Bardina, J., Ferziger, J. H., & W. J., Reynolds, W. C., 1983, *Rept. TF-19*, Dept. Mech. Eng., Stanford U.
- Canuto, C., Hussaini, M. Y., Quarteroni, A., & Zang, T. A., 1988, *Spectral Methods in Fluid Dynamics* Springer-Verlag, New York.
- Dahlburg, J. P., Dahlburg, R. B., Gardner, J. H., & Picone, J. M. 1990, *Phys. Fluids A* 2, 1481-1486.
- Dahlburg, R. B., & Picone, J. M. 1989, *Phys. Fluids B*, 1, 2153-2171.
- Erlebacher, G., Hussaini, M. Y., Kreiss, H. O., & Sarkar, S. 1990a, *ICASE tech. rept. 90-15*.
- Erlebacher, G., Hussaini, M. Y., Speziale, C. G., & Zang, T. A. 1990b, *submitted*.
- Feiereisen, W. J., Reynolds, W. C., & Ferziger, J. H., 1981, *Rept. TF-13*, Dept. Mech. Eng., Stanford U.
- Gauthier, S. 1988, *J. Comp. Phys.* 75, 217-235.
- Grappin, R., Leorat, J., & Londrillo, P. 1988, *J. Fluid Mech.* 195, 239-256.
- Henshaw, W. D., Kreiss, H. O., & Reyna, L. G., 1989, *Theor. Comp. Fluid Dyn.* 1, 65.
- Hossain, M., & Mullan, D. J., 1990, *Astrophys. J.* 354, L33.
- Moin, P., & Kim, J., 1982, *J. Fluid Mech.* 118, 341-377.
- Passot, T., & Pouquet, A., 1988, *J. Fluid Mech.* 181, 441-466.
- Passot, T., & Pouquet, A., 1988, *J. Comp. Phys.* 75, 300.
- Picone, J. M., & Dahlburg, R. B., 1991, *Phys. Fluids B*, 3, 29-44.
- Piomelli, U., Ferziger, J. H., & Moin, P., 1989, *Phys. Fluids A* 1, 1061-1068.
- Reynolds, W. C., 1990, in *Whither Turbulence?*, Lecture Notes in Physics 357, pp. 313-343, Springer, Berlin.

- Rogallo, R. S., & Moin, P., 1984, *Ann. Rev. Fluid Mech.* 16, 99.
- Sakell, L., 1988, *Naval Research Lab. memo rept.* 6153.
- Sarkar, S., Erlebacher, G., Hussaini, M. Y., & Kreiss, H. O., 1989, *ICASE tech. rept.* 89-79.
- Sarkar, S., & Balakrishnan, L., 1990, *ICASE tech. rept.* 90-18.
- Speziale, C. G., 1991, *Ann. Rev. Fluid Mech.* 23, in press.
- Speziale, C. G., Erlebacher, G., Zang, T. A., & Hussaini, M. Y. 1988, *Phys. Fluids* 31, 940-942.
- Staroselsky, I., Yakhot, V., Kida, S., & Orszag, S. A., 1990, *Phys. Rev. Lett.* 65, 171-174.
- Yoshizawa, A. 1986, *Phys. Fluids* 29, 2152-2164.

TABLE I.

Case	M_a	χ	T'	Re	k_0	E_0/ϵ_0
QIC01	0.1	0.0		22.74		1.85
QIC04	0.4	0.0		22.74		1.86
M01C00	0.1	0.0	0.0000	250.0	10	1.18
M01C02	0.1	0.2	0.0626	250.0	10	1.11
M01C04	0.1	0.4	0.0881	250.0	10	1.04
M01C06	0.1	0.6	0.1082	250.0	10	0.98
M01C08	0.1	0.8	0.1252	250.0	10	0.93
M02C02	0.2	0.2	0.1191	250.0	10	1.11
M03C02	0.3	0.2	0.1663	250.0	10	1.11
M01C02K5	0.1	0.2	0.0626	250.0	5	5.19
M01C02K5R	0.1	0.2	0.0626	125.0	5	2.59

TABLE II. LES Runs (Standard Case)

Run	<i>s.s.model</i>	C_R	C_I	C_T	<i>Delta</i>
M01C02a	<i>on</i>	.0120	.00660	.0170	2
M01C02b	<i>off</i>	.0120	.00660	.0170	2
M01C02c	<i>on</i>	.0000	.00000	.0000	2
M01C02d	<i>on</i>	.0132	.00726	.0189	2
M01C02e	<i>on</i>	.0108	.00594	.0154	2
M01C02f	<i>on</i>	.0120	.00000	.0170	2
M01C02g	<i>on</i>	.0108	.00660	.0154	2
M01C02h	<i>on</i>	.0120	.00660	.0170	1
M01C02i	<i>on</i>	.0120	.00660	.0170	4
M01C02j	<i>on</i>	.0108	.00000	.0077	2
M01C02k	<i>on</i>	.0108	.00000	.0231	2
M01C02l	<i>on</i>	.0108	.00000	.0034	2
M01C02m	<i>on</i>	.0120	.06600	.0170	2
M01C02n	<i>on</i>	.0120	.33000	.0170	2
M01C02o	<i>on</i>	.0108	.33000	.0154	2
M01C02p	<i>on</i>	.0108	.33000	.0230	2

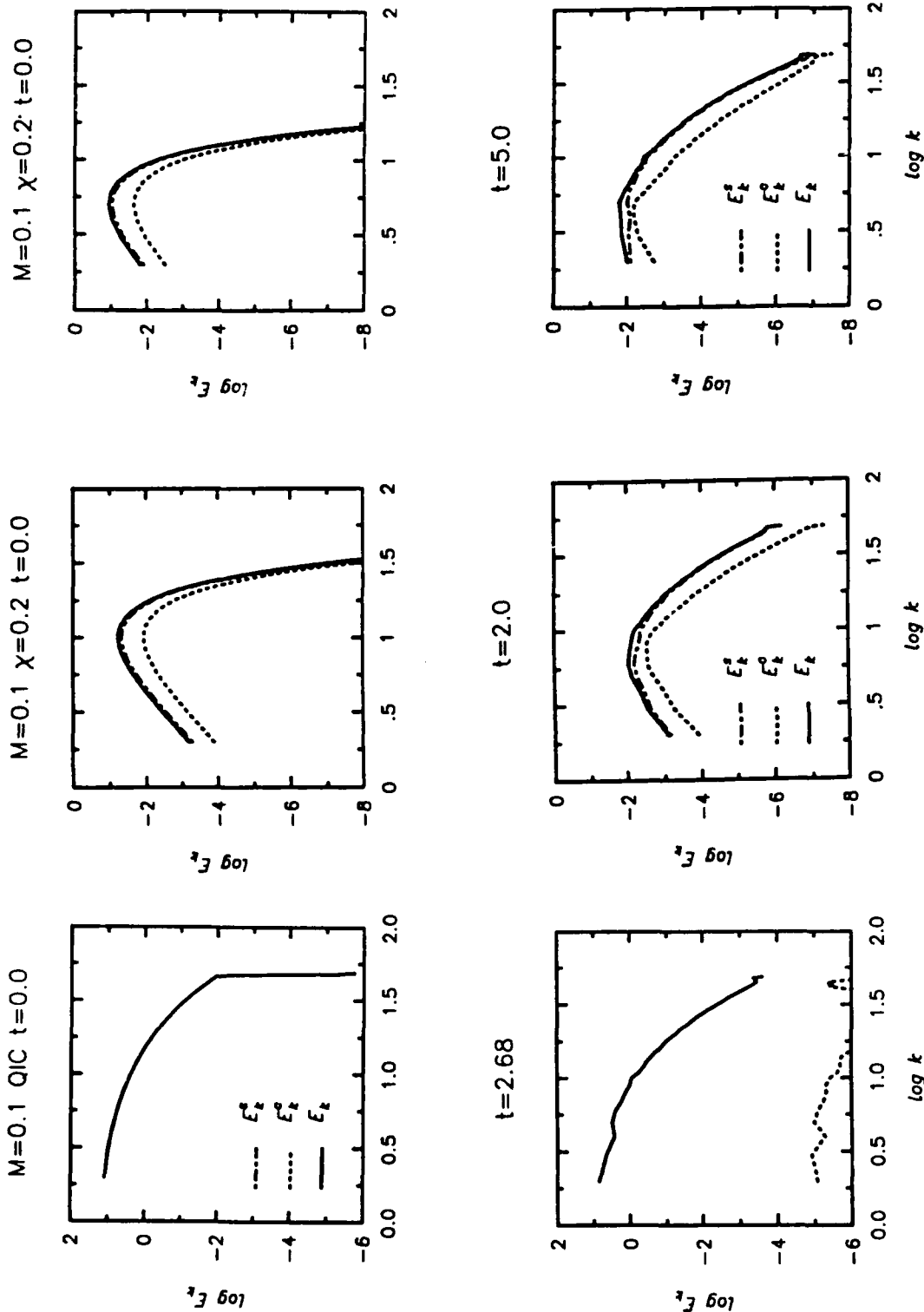


Fig. 1 — Energy spectra for three DNS of compressible turbulence. The spectra of the total kinetic energy (per unit mass), E , its incompressible component, E^i , and its compressible component, E^c , are shown. Both the initial spectra (top) and a fully developed spectra (bottom) are given for the cases QIC01, M01C02 and M01C02K5.

$M=0.1$ QIC

$Re=22.74$ 96^3 DNS

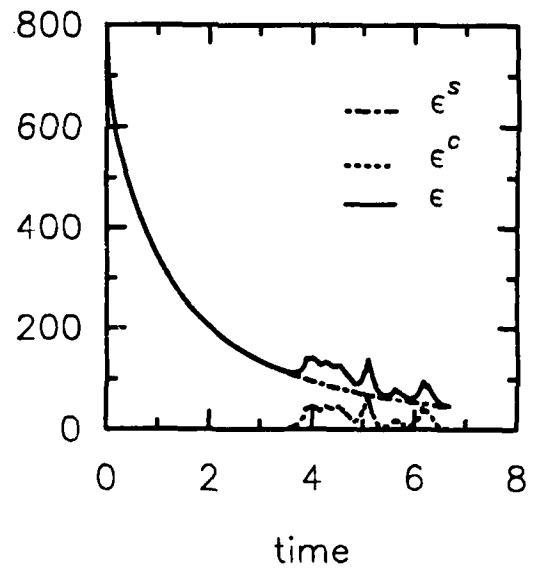
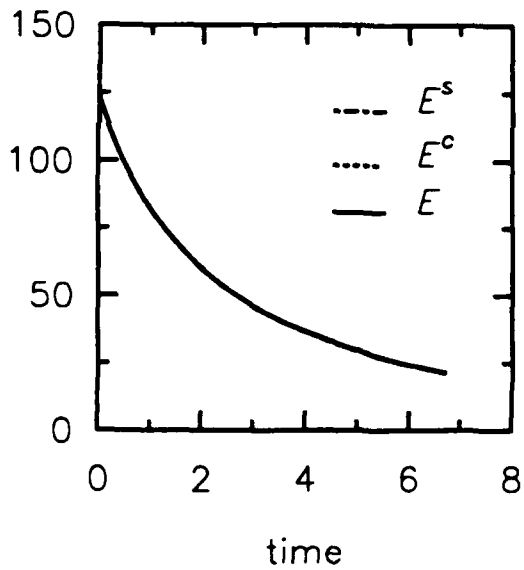
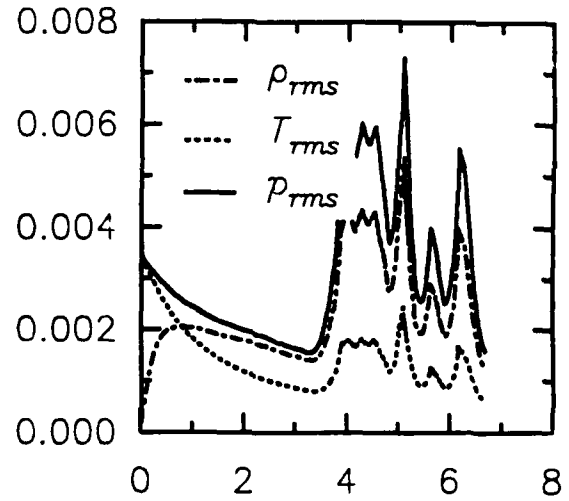
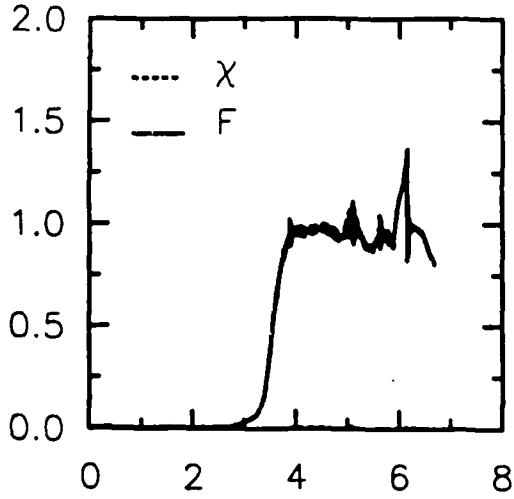


Fig. 2 — Time evolution of key diagnostics for 96^3 DNS run QIC01: (a) χ and F ; (b) ρ_{rms} , T_{rms} and p_{rms} ; (c) E^s , E^c , and E ; and (d) ϵ^s , ϵ^c , and ϵ .

$M=0.4$ QIC

$Re=22.74$ 96^3 DNS

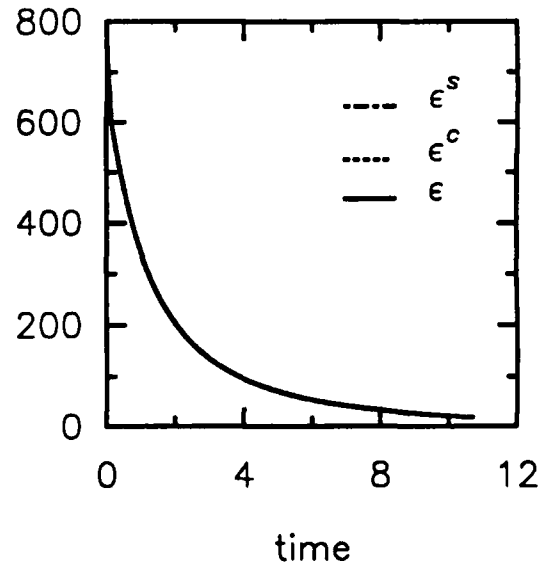
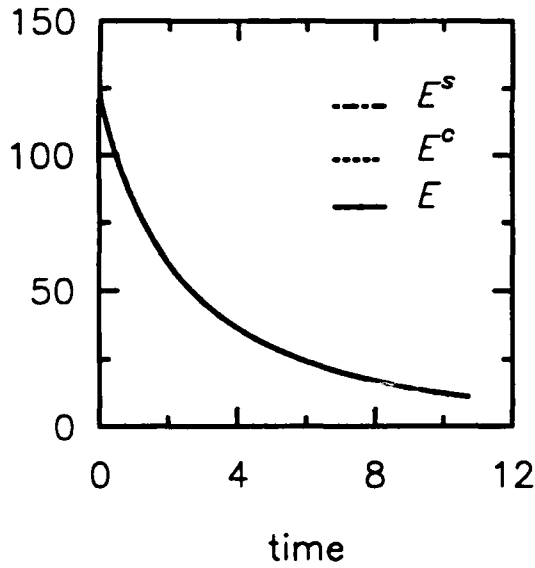
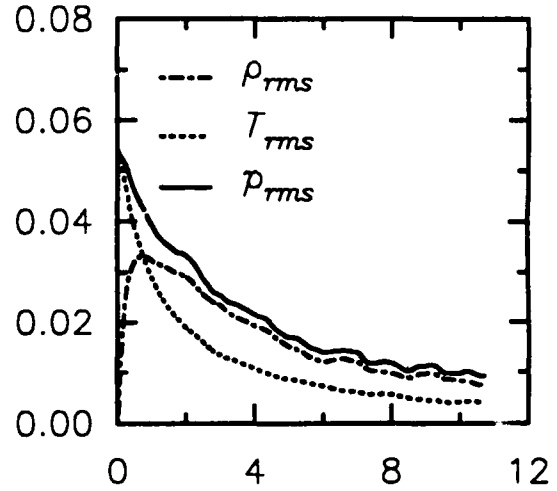
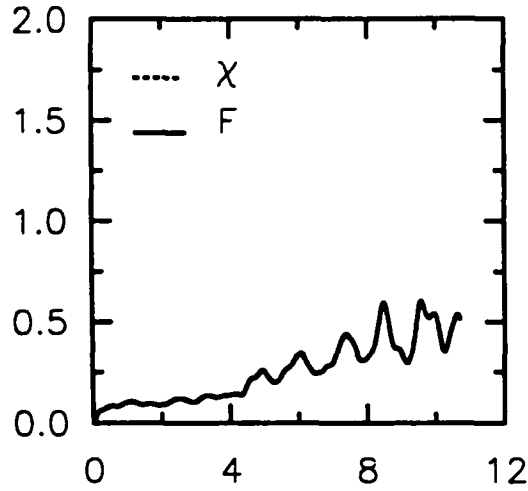


Fig. 3 — Time evolution of key diagnostics for 96^3 DNS run QIC04: (a) χ and F ; (b) ρ_{rms} , P_{rms} , and T_{rms} ; (c) E^s , E^c , and E ; and (d) ϵ^s , ϵ^c , and ϵ .

$M=0.1 \quad \chi=0.0 \quad k_0=10$

$Re=250 \quad 96^3 \text{ DNS}$

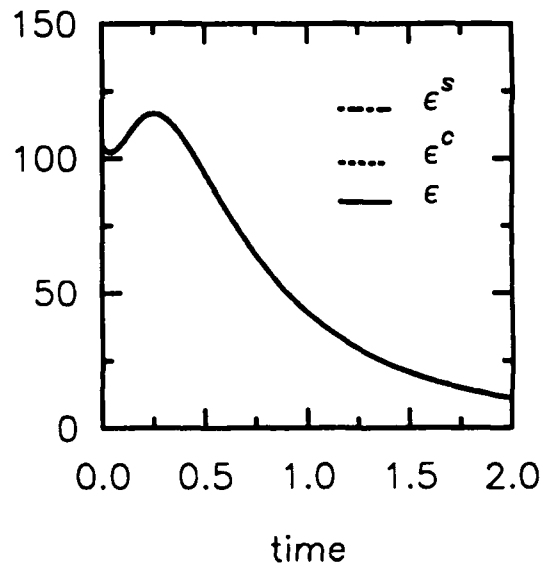
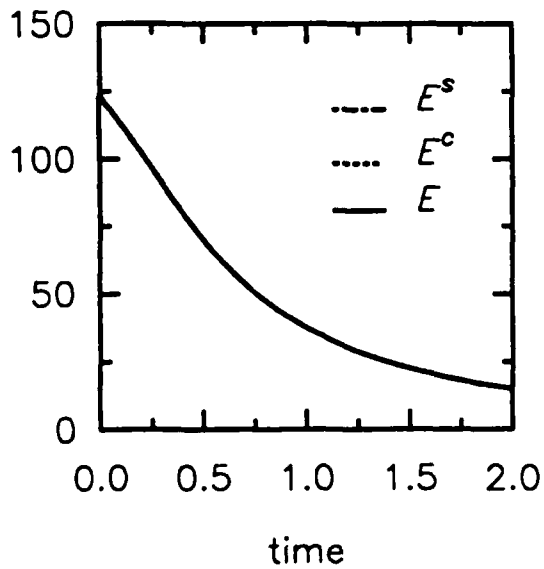
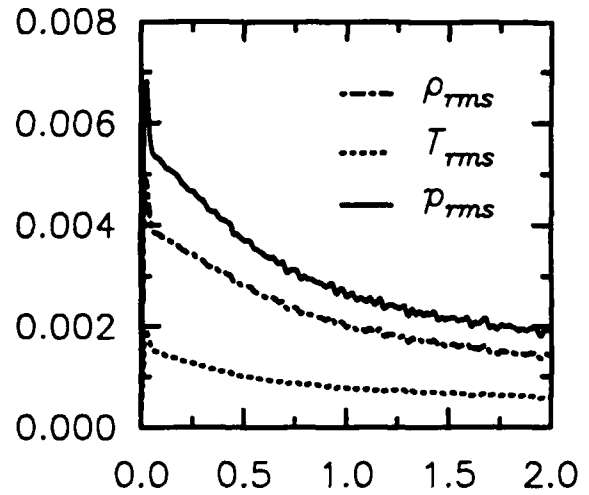
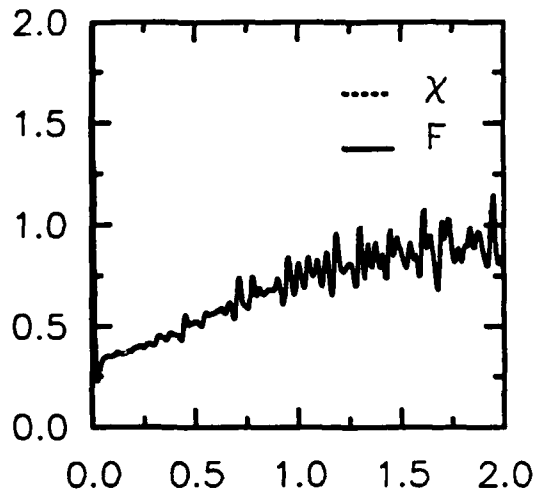


Fig. 4 — Time evolution of key diagnostics for 96^3 DNS run M01C00: (a) χ and F ; (b) ρ_{rms} , p_{rms} , and T_{rms} ; (c) E^s , E^c , and E ; and (d) ϵ^s , ϵ^c , and ϵ .

$M=0.1 \quad \chi=0.2 \quad k_0=10$

$Re=250 \quad 96^3 \text{ DNS}$

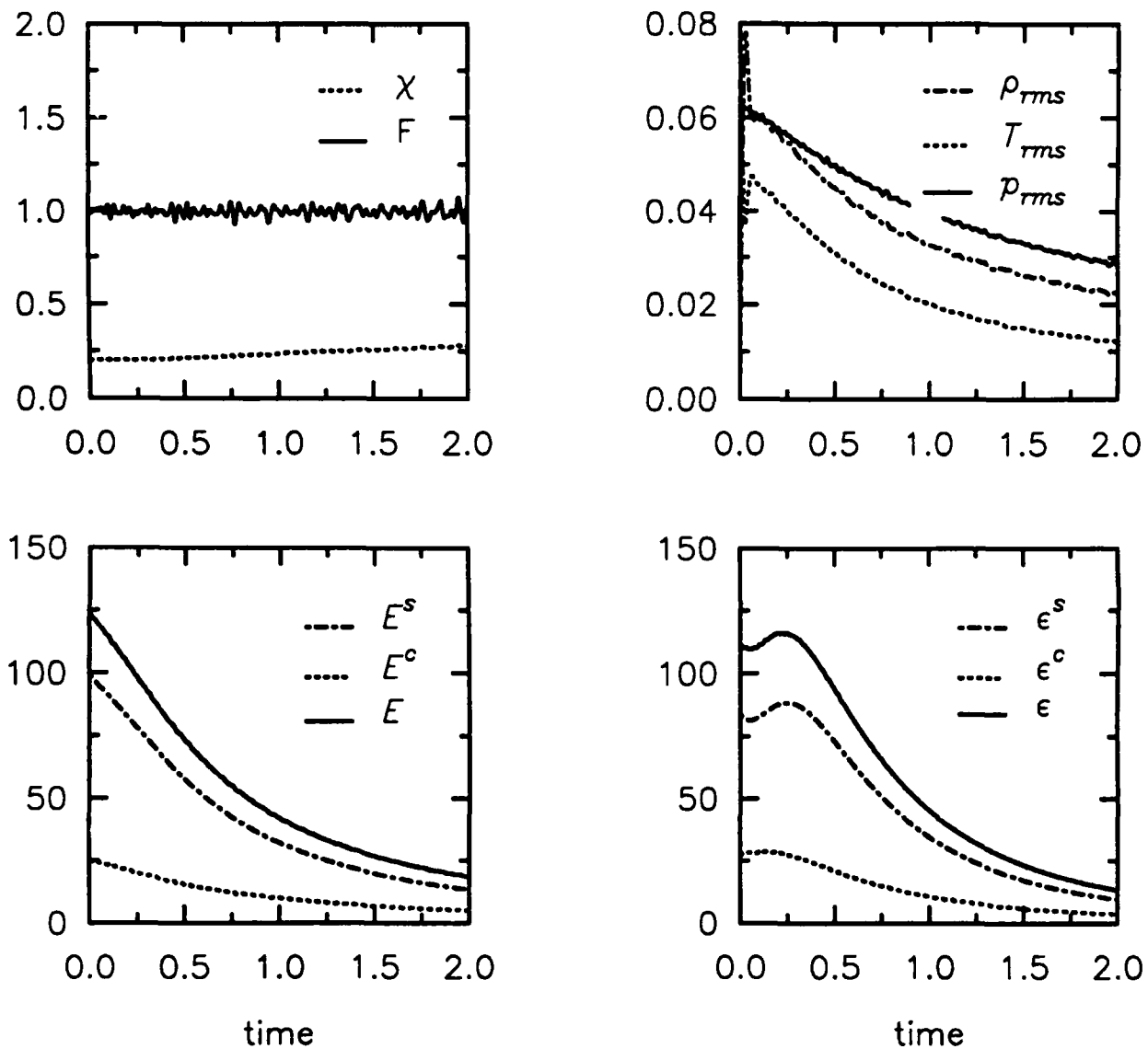


Fig. 5 — Time evolution of key diagnostics for 96^3 DNS run M01C02: (a) χ and F ; (b) ρ_{rms} , p_{rms} , and T_{rms} ; (c) E^s , E^c , and E ; and (d) ϵ^s , ϵ^c , and ϵ .

$M=0.1 \quad \chi=0.4 \quad k_0=10$

$Re=250 \quad 96^3 \text{ DNS}$

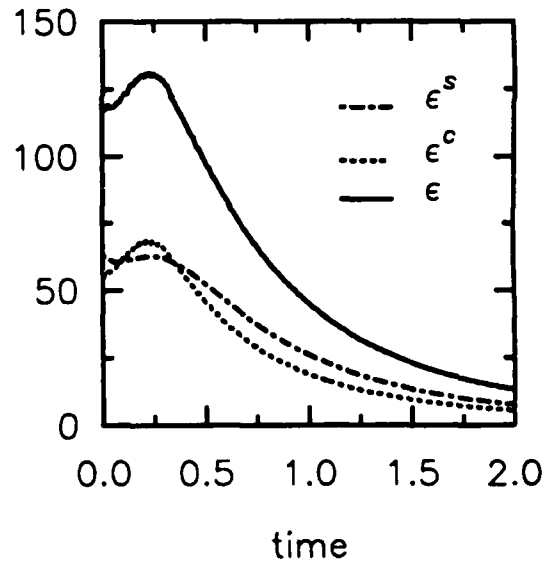
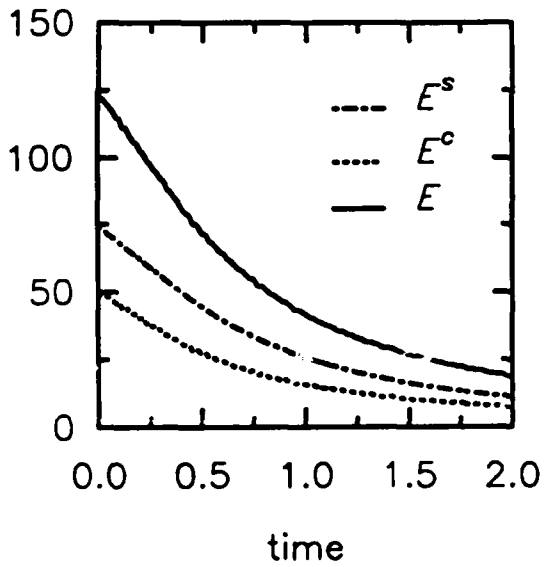
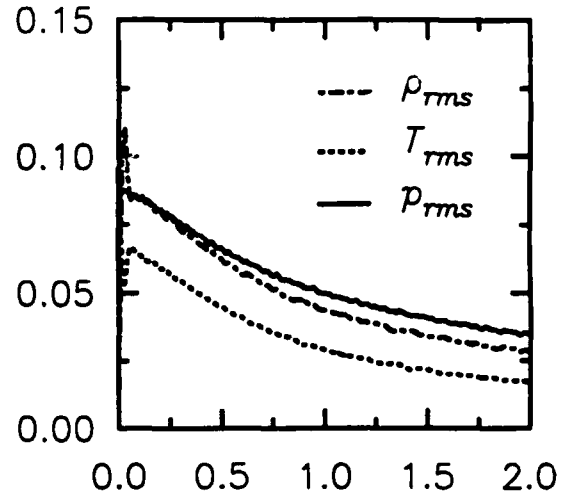
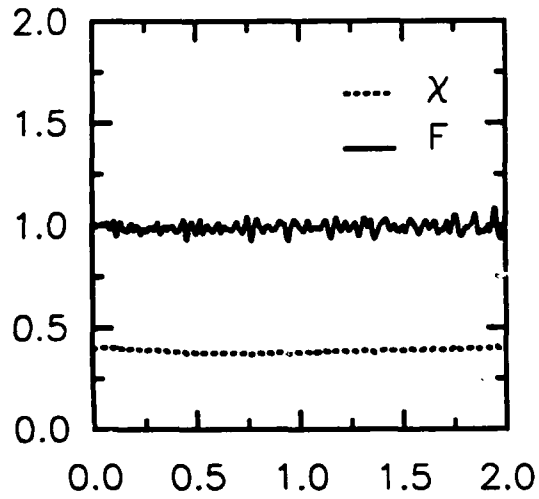


Fig. 6 — Time evolution of key diagnostics for 96^3 DNS run M01C04: (a) χ and F ; (b) ρ_{rms} , P_{rms} , and T_{rms} ; (c) E^s , E^c , and E ; and (d) ϵ^s , ϵ^c , and ϵ .

$M=0.1 \quad \chi=0.6 \quad k_0=10$

$Re=250 \quad 96^3 \text{ DNS}$

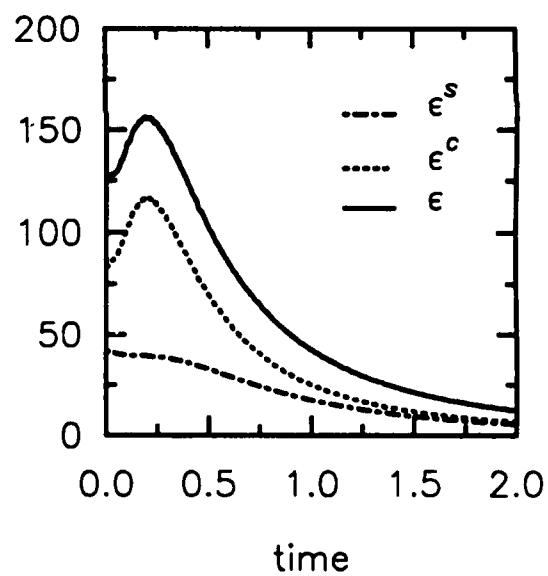
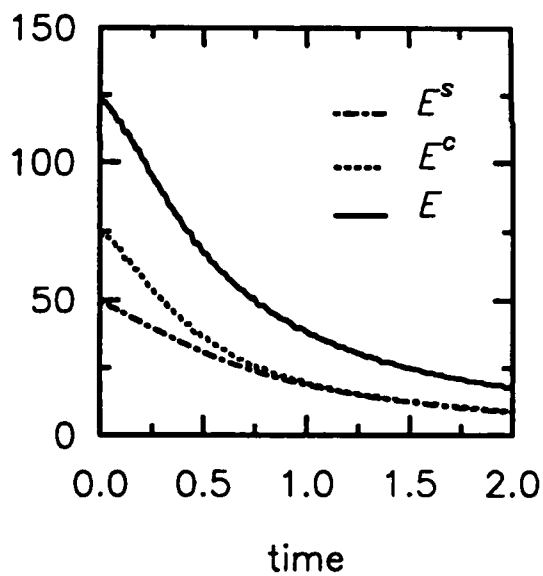
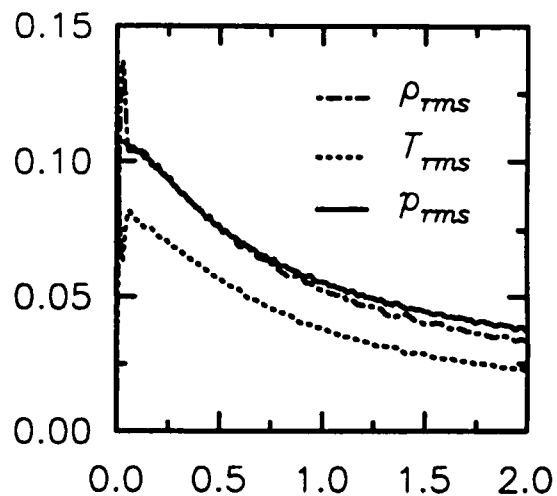
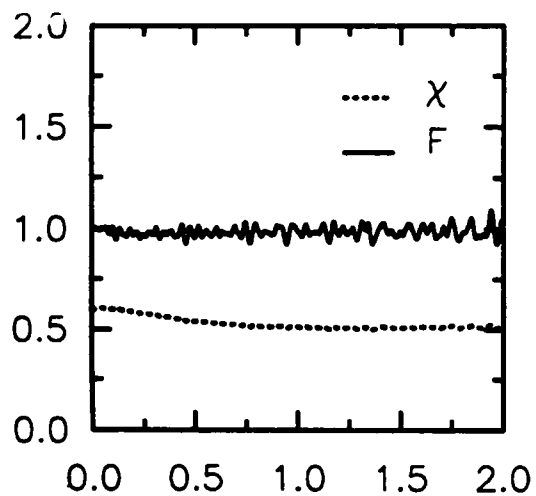


Fig. 7 — Time evolution of key diagnostics for 96^3 DNS run M01C06: (a) χ and F ; (b) ρ_{rms} , p_{rms} , and T_{rms} ; (c) E^s , E^c , and E ; and (d) ϵ^s , ϵ^c , and ϵ .

$M=0.1 \quad \chi=0.8 \quad k_0=10$

$Re=250 \quad 96^3 \text{ DNS}$

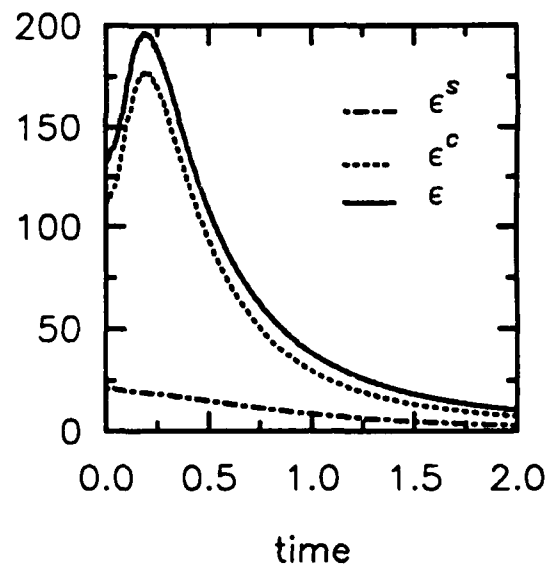
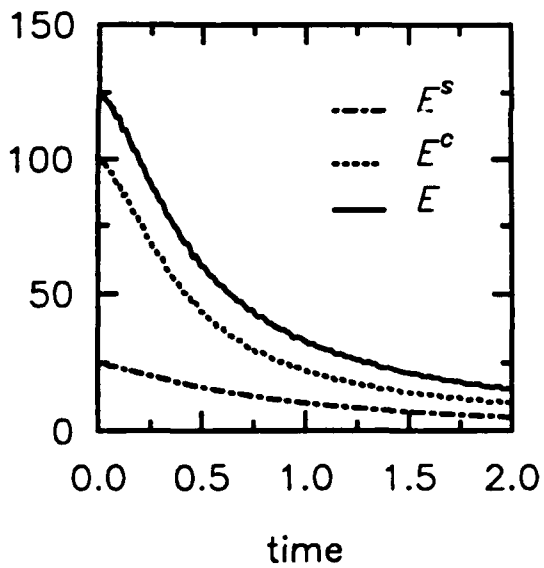
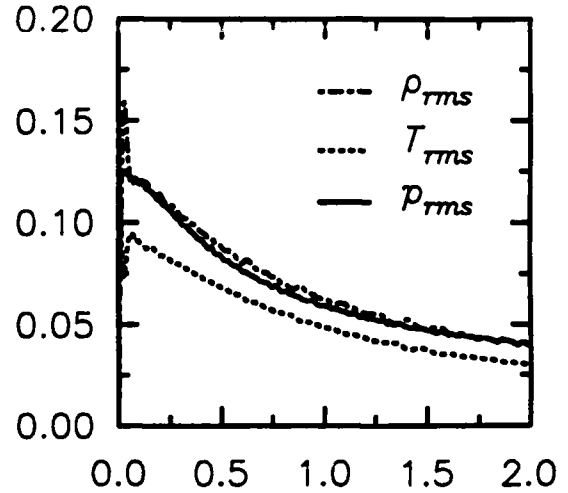
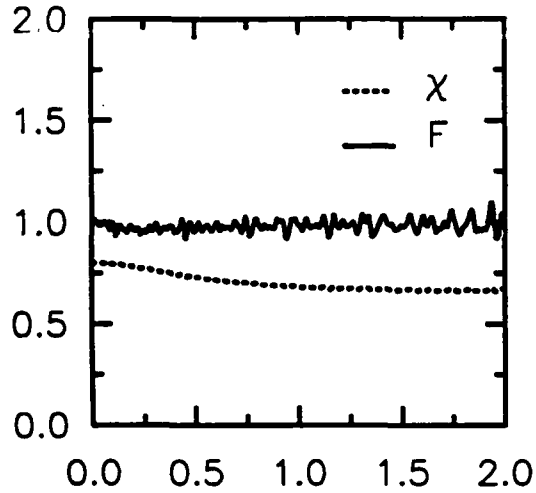


Fig. 8 — Time evolution of key diagnostics for 96^3 DNS run M01C08: (a) χ and F ; (b) ρ_{rms} , P_{rms} , and T_{rms} ; (c) E^s , E^c , and E ; and (d) ϵ^s , ϵ^c , and ϵ .

$M=0.2 \quad \chi=0.2 \quad k_0=10$

$Re=250 \quad 96^3 \text{ DNS}$

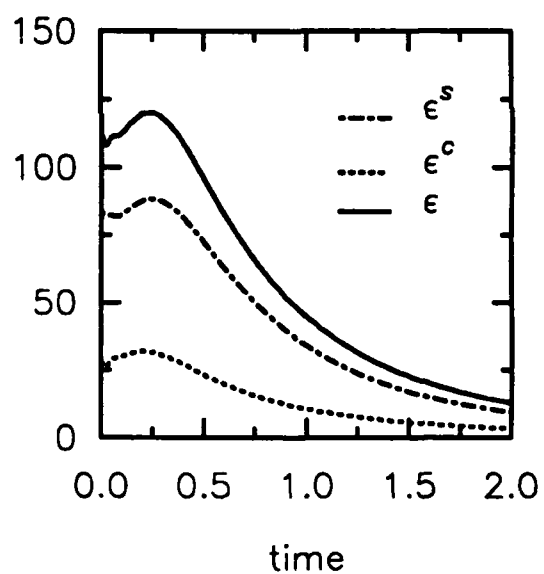
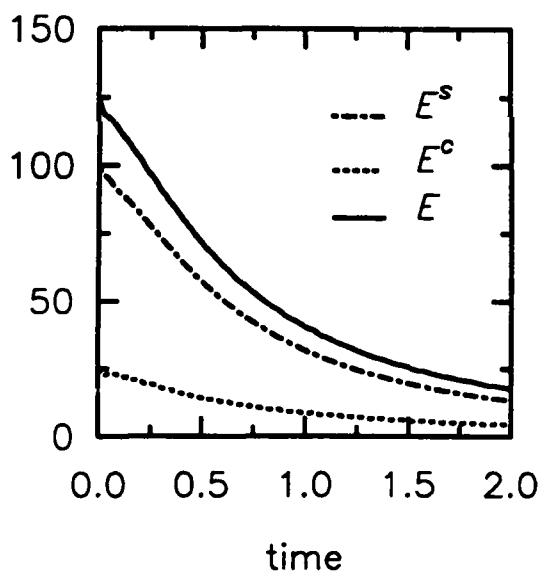
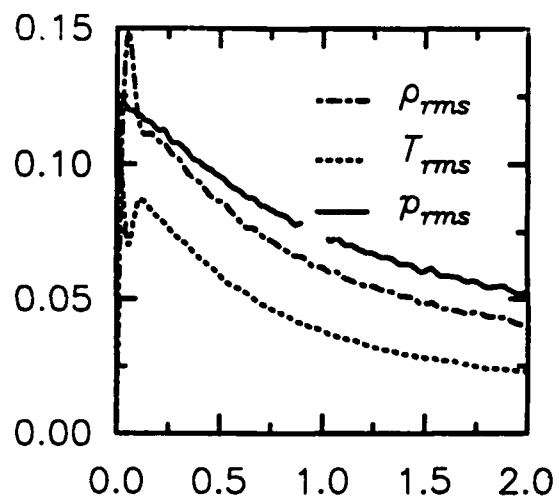
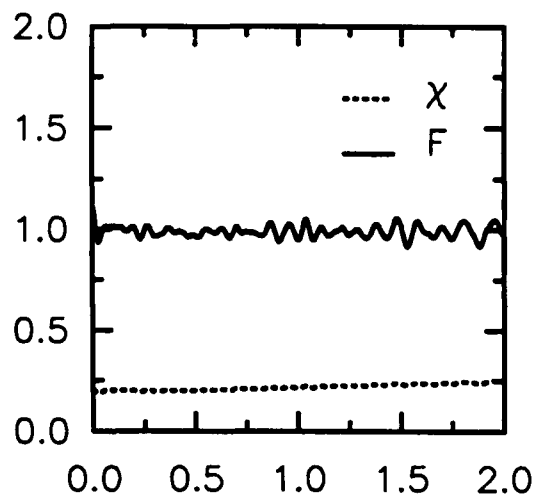


Fig. 9 — Time evolution of key diagnostics for 96^3 DNS run M02C02: (a) χ and F ; (b) ρ_{rms} , p_{rms} , and T_{rms} ; (c) E^s , E^c , and E ; and (d) ϵ^s , ϵ^c , and ϵ .

$M=0.3 \quad \chi=0.2 \quad k_0=10$

$Re=250 \quad 96^3 \text{ DNS}$

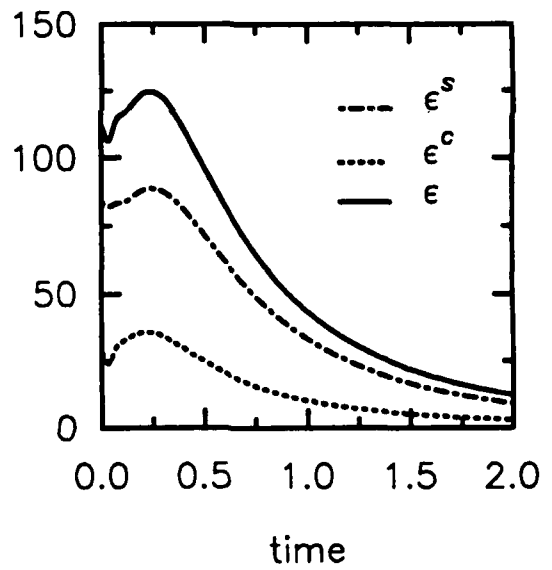
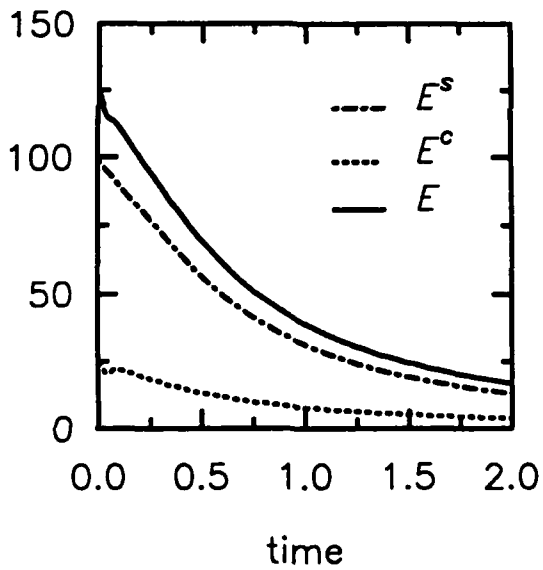
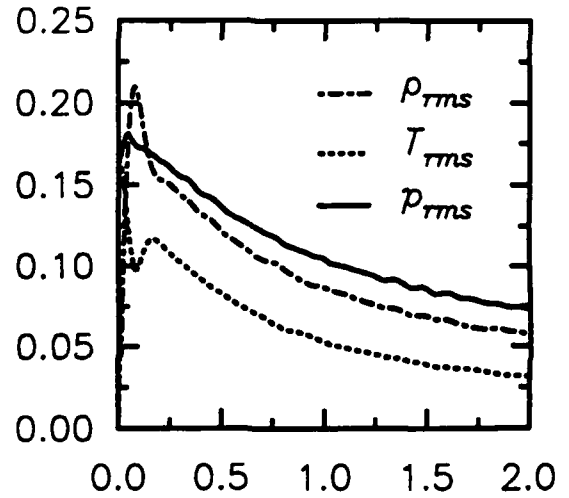
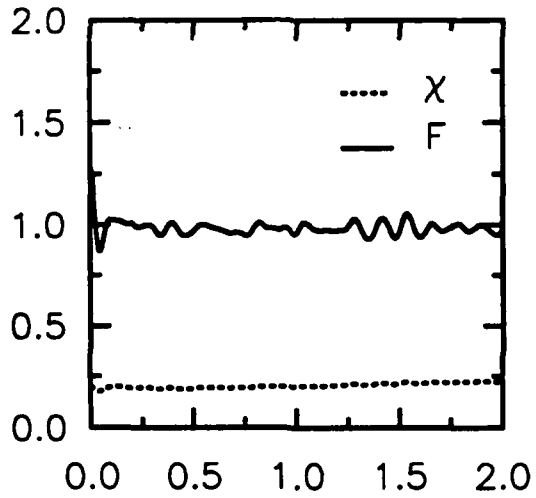


Fig. 10 — Time evolution of key diagnostics for 96^3 DNS run M03C02: (a) χ and F ; (b) ρ_{rms} , p_{rms} , and T_{rms} ; (c) E^s , E^c , and E ; and (d) ϵ^s , ϵ^c , and ϵ .

$M=0.1 \quad \chi=0.2 \quad k_0=5$

$Re=250 \quad 96^3 \text{ DNS}$

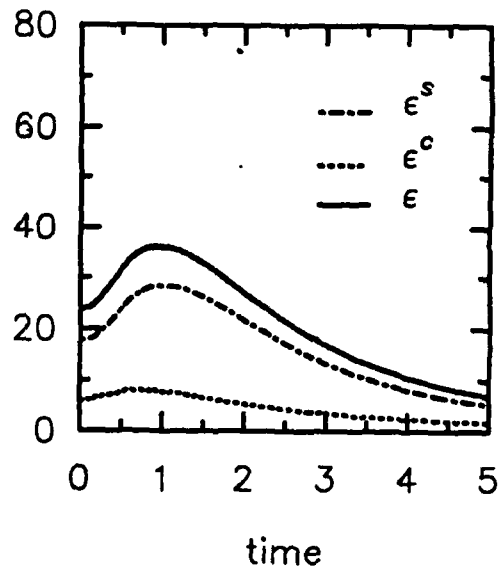
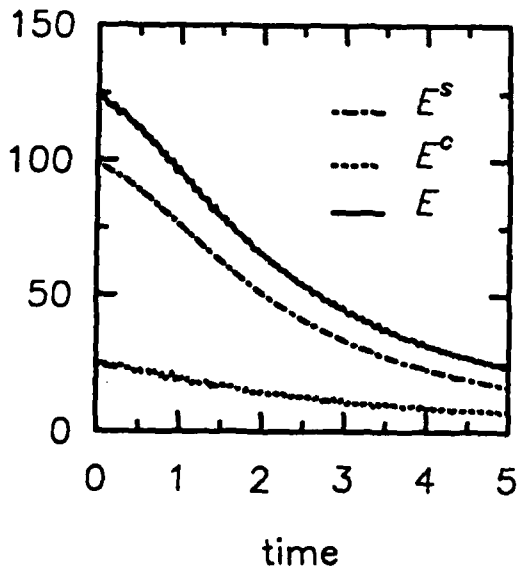
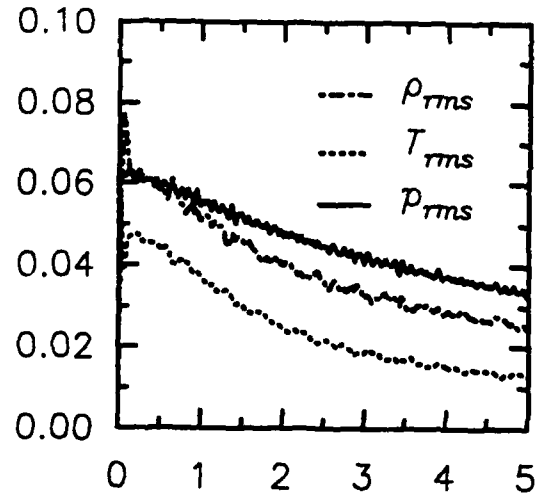
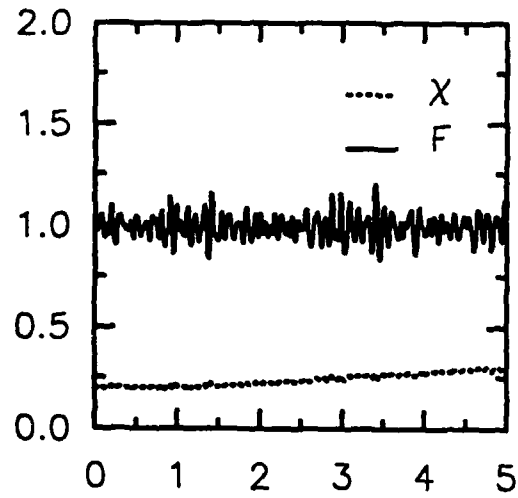


Fig. 11 — Time evolution of key diagnostics for 96^3 DNS run M01C02K5: (a) χ and F ; (b) ρ_{rms} , P_{rms} , and T_{rms} ; (c) E^s , E^c , and E ; and (d) ϵ^s , ϵ^c , and ϵ .

$M=0.1 \quad \chi=0.2 \quad k_0=5$

$Re=125 \quad 96^3 \text{ DNS}$

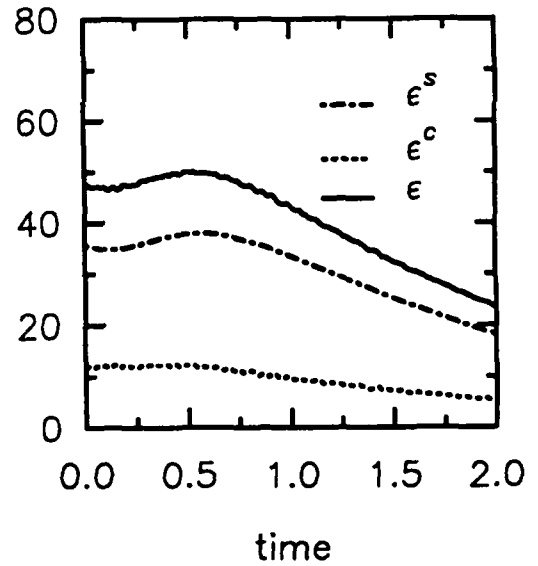
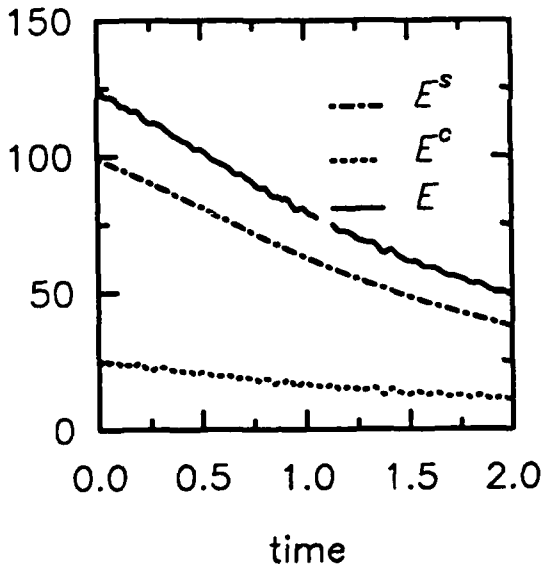
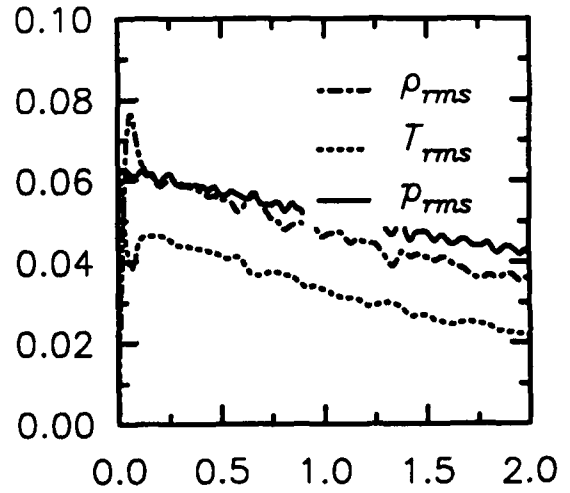
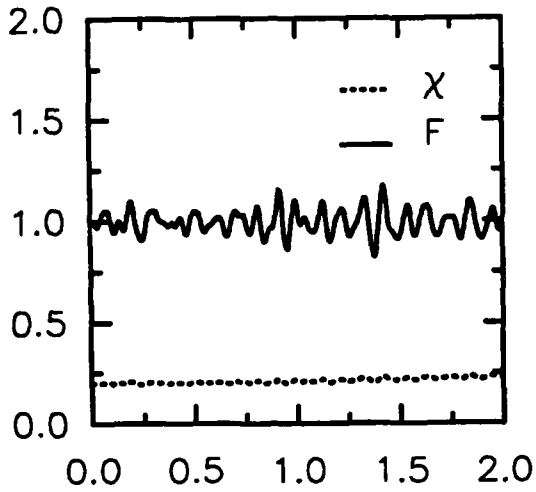


Fig. 12 — Time evolution of key diagnostics for 96^3 DNS run M01C02K5R: (a) χ and F ; (b) ρ_{rms} , p_{rms} , and T_{rms} ; (c) E^s , E^c , and E ; and (d) ϵ_s , ϵ^c , and ϵ .

$M=0.1$ QIC

$Re=22.74$ 96^3 DNS

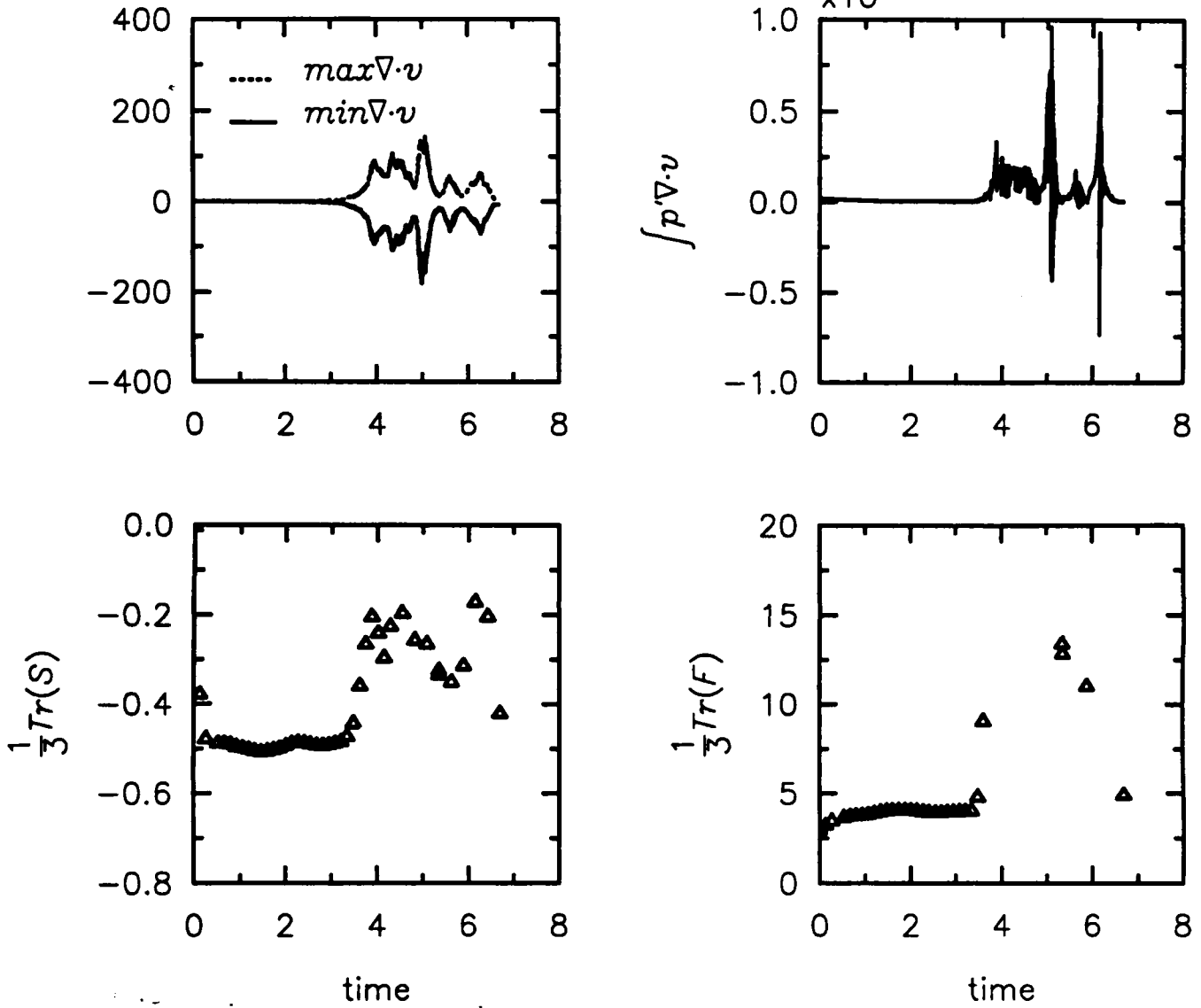


Fig. 13 — Time evolution of additional key diagnostics for 96^3 DNS run QIC01: (a) min and max $\nabla \cdot v$; (b) pressure dilatation; (c) skewness; and (d) flatness.

$M=0.1 \quad \chi=0.2 \quad k_0=10$

$Re=250 \quad 96^3 \text{ DNS}$

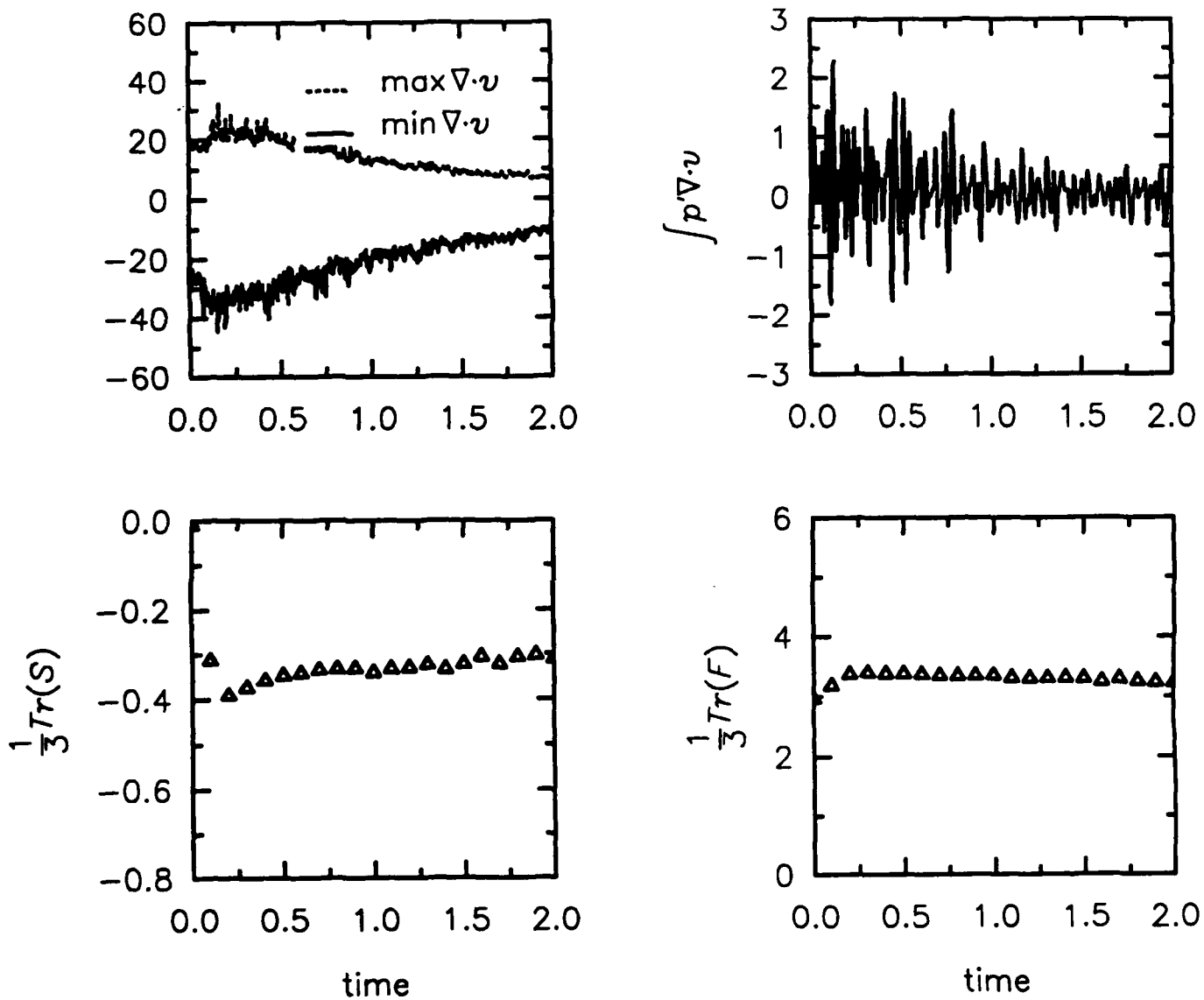


Fig. 14 — Time evolution of additional key diagnostics for 96^3 DNS run M01C02: (a) min and max $\nabla \cdot v$; (b) pressure dilatation; (c) skewness; and (d) flatness

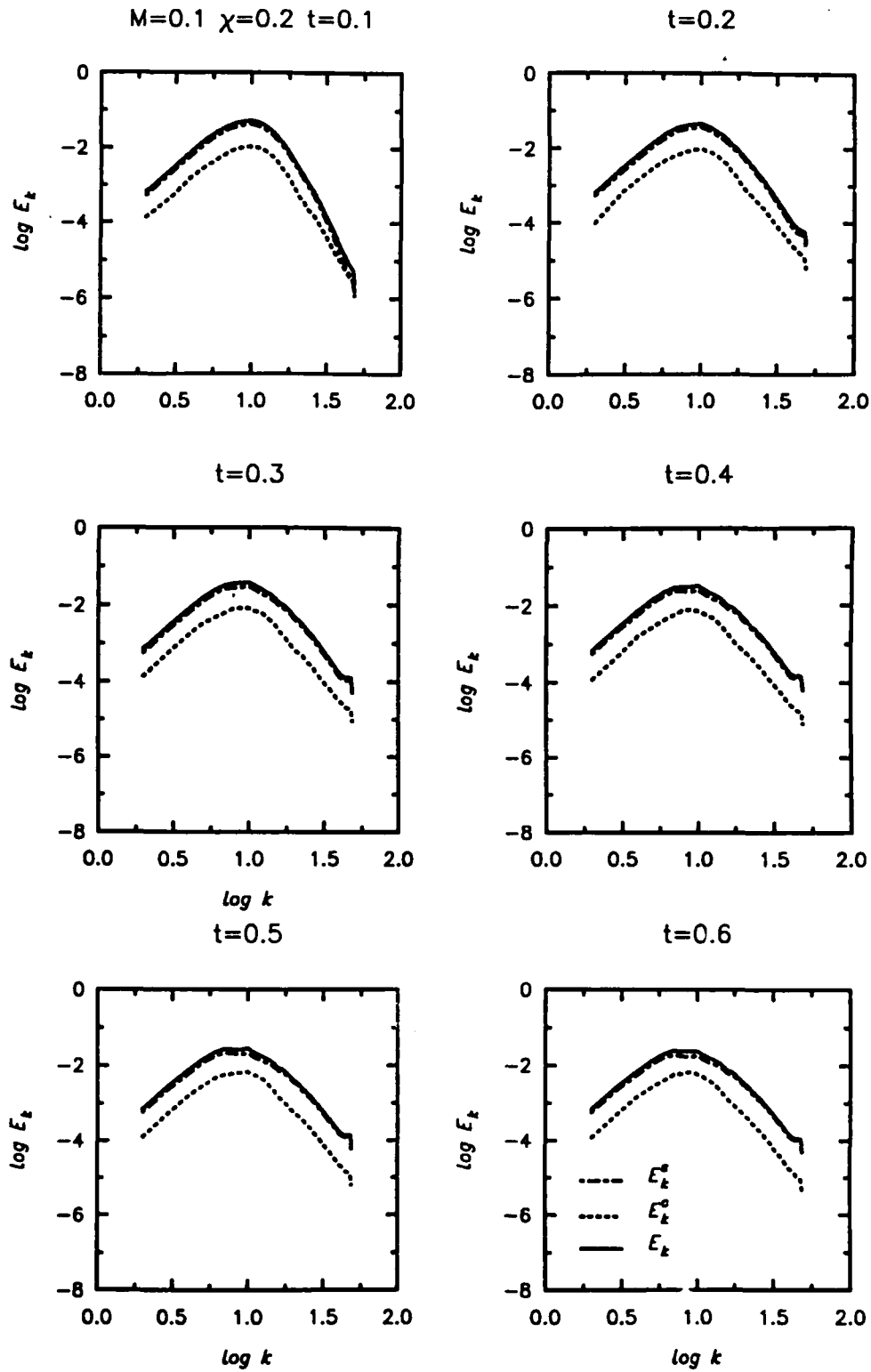


Fig. 15 — Energy spectra for 96^3 DNS run M01C02: (a) $t = 0.1$; (b) $t = 0.2$; (c) $t = 0.3$; (d) $t = 0.4$; (e) $t = 0.5$; and (f) $t = 0.6$.

$M=0.1$ QIC

standard model

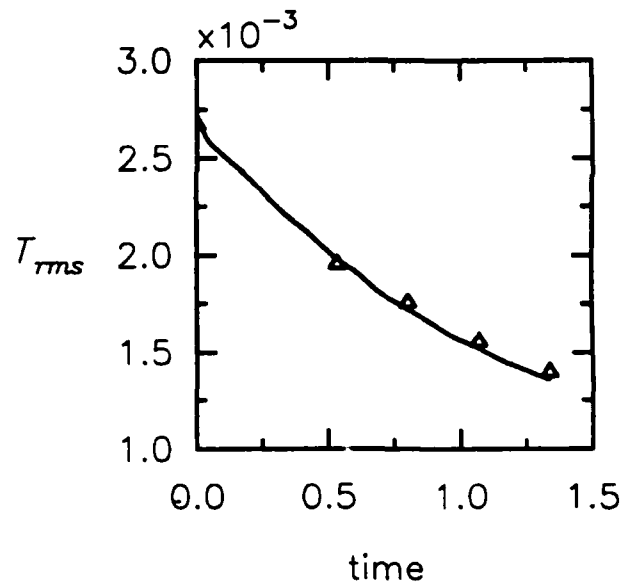
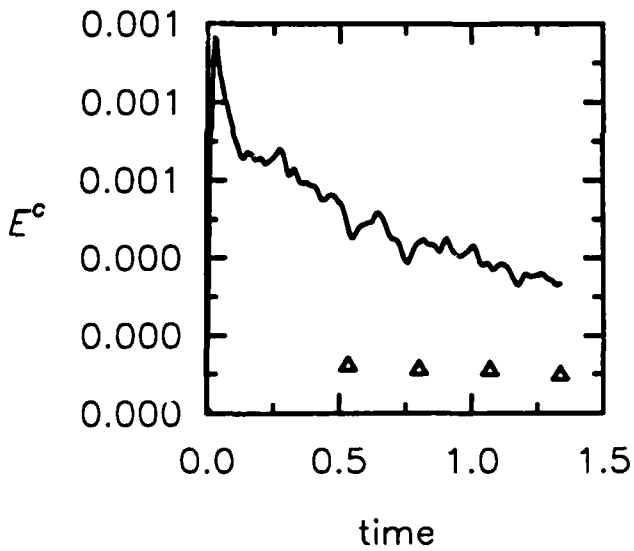
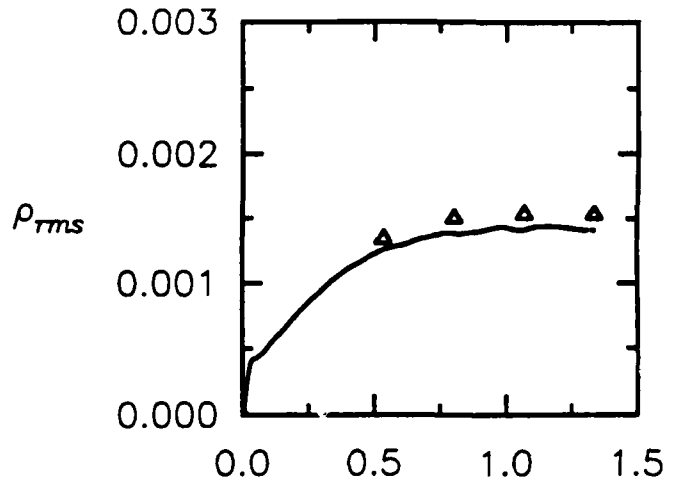
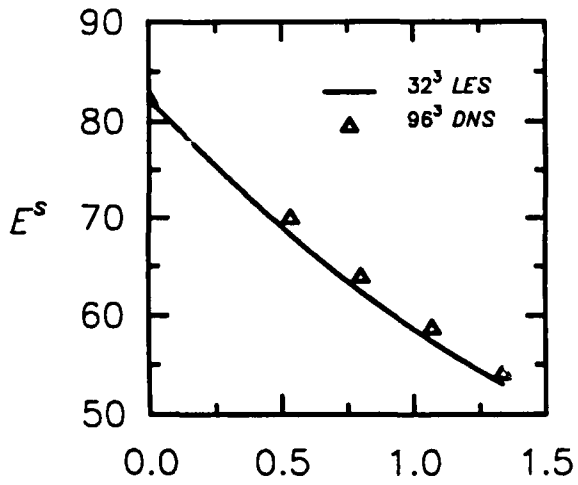


Fig. 16 — LES on a 32^3 grid of the case QIC01 using the *SEZHu* model with its recommended constants. The results are compared with a well-resolved, 96^3 DNS

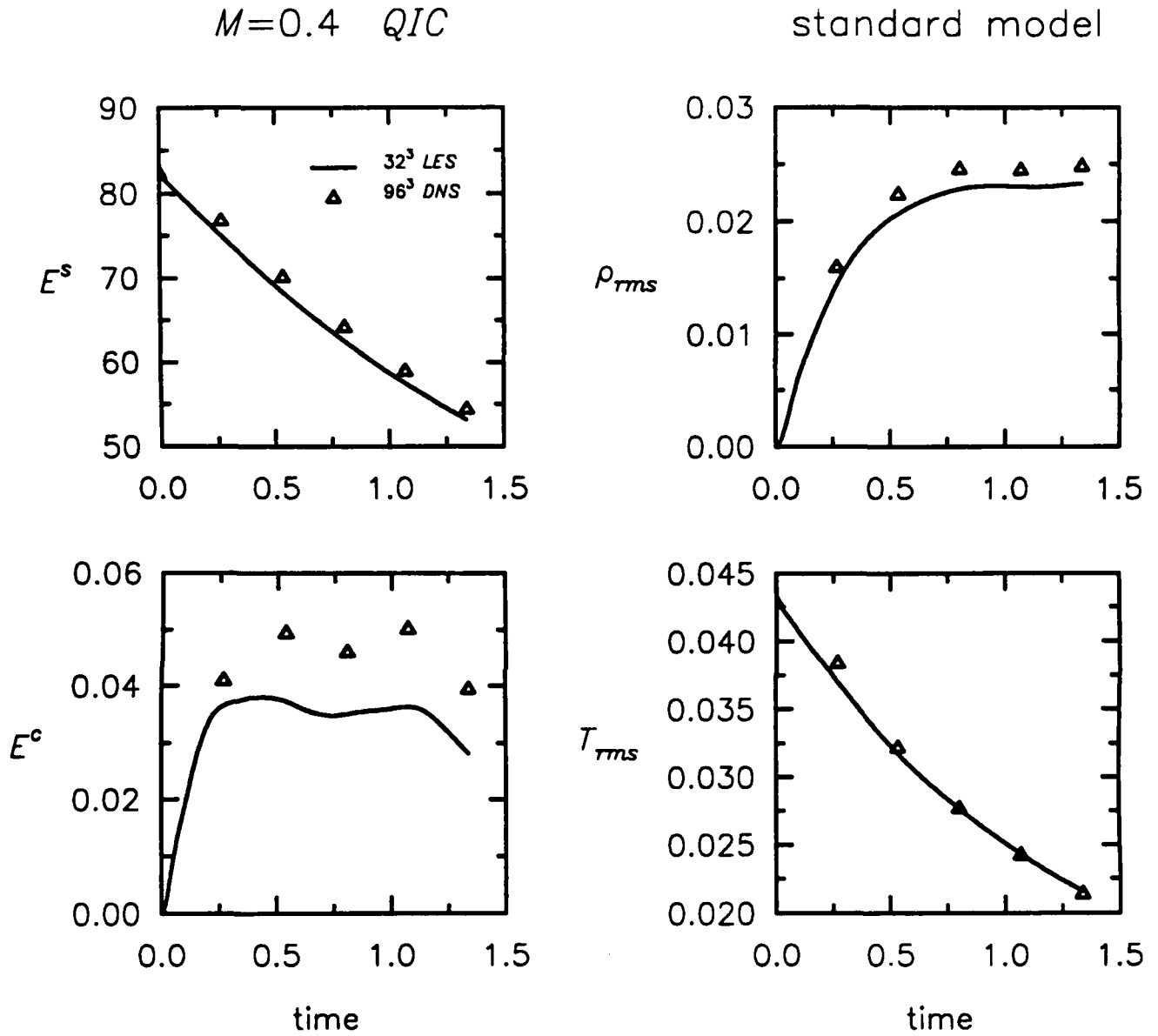


Fig. 17 — LES on a 32^3 grid of the case QIC04 using the *SEZHu* model with its recommended constants. The results are compared with a well-resolved, 96^3 DNS

$M=0.1 \quad \chi=0.0$

standard model

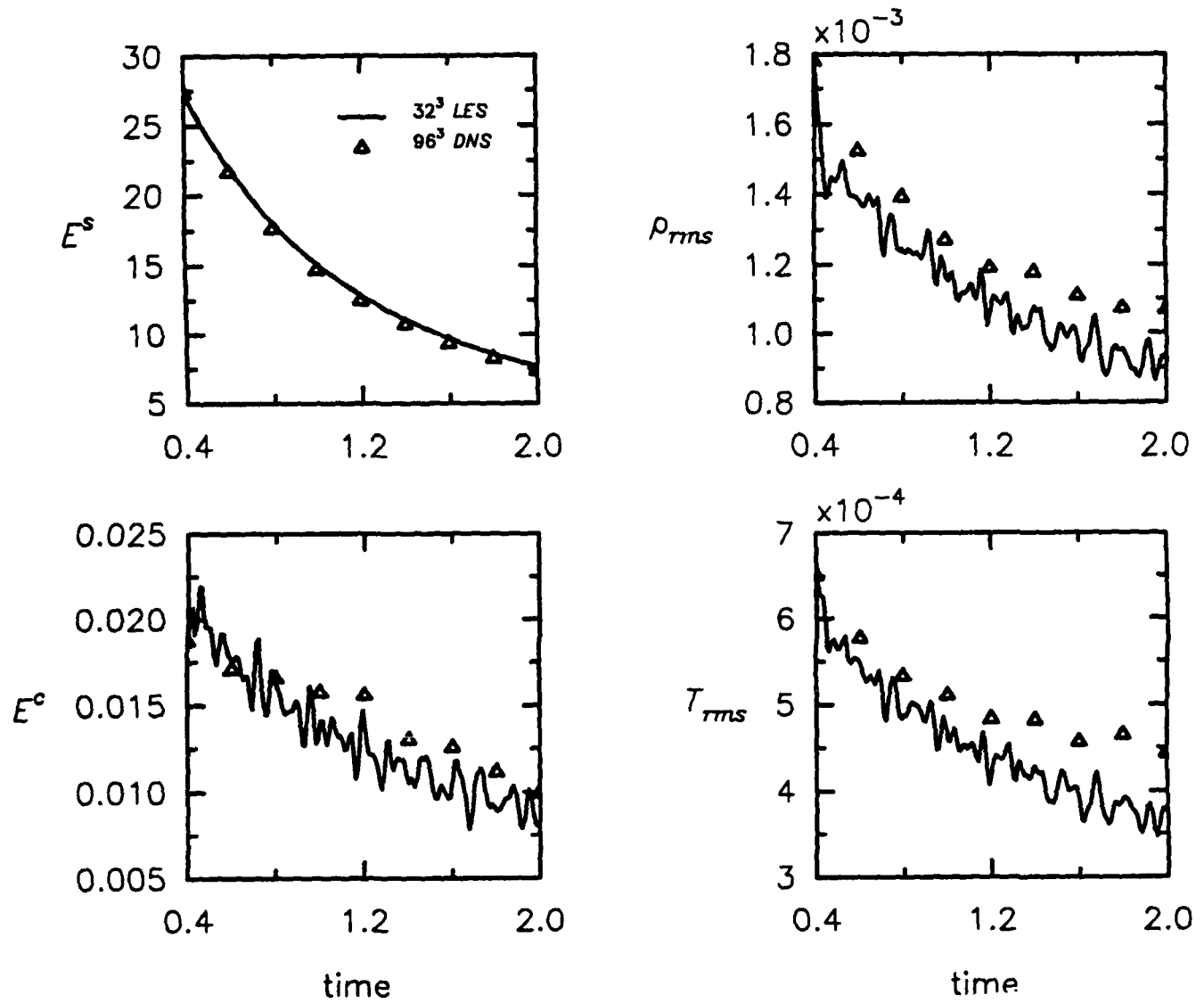


Fig. 18 —LES on a 32^3 grid of the case M01C00 using the *SEZHu* model with its recommended constants. The results are compared with a well-resolved, 96^3 DNS

$M=0.1$ $\chi=0.2$

100% C_R 100% C_I 100% C_T

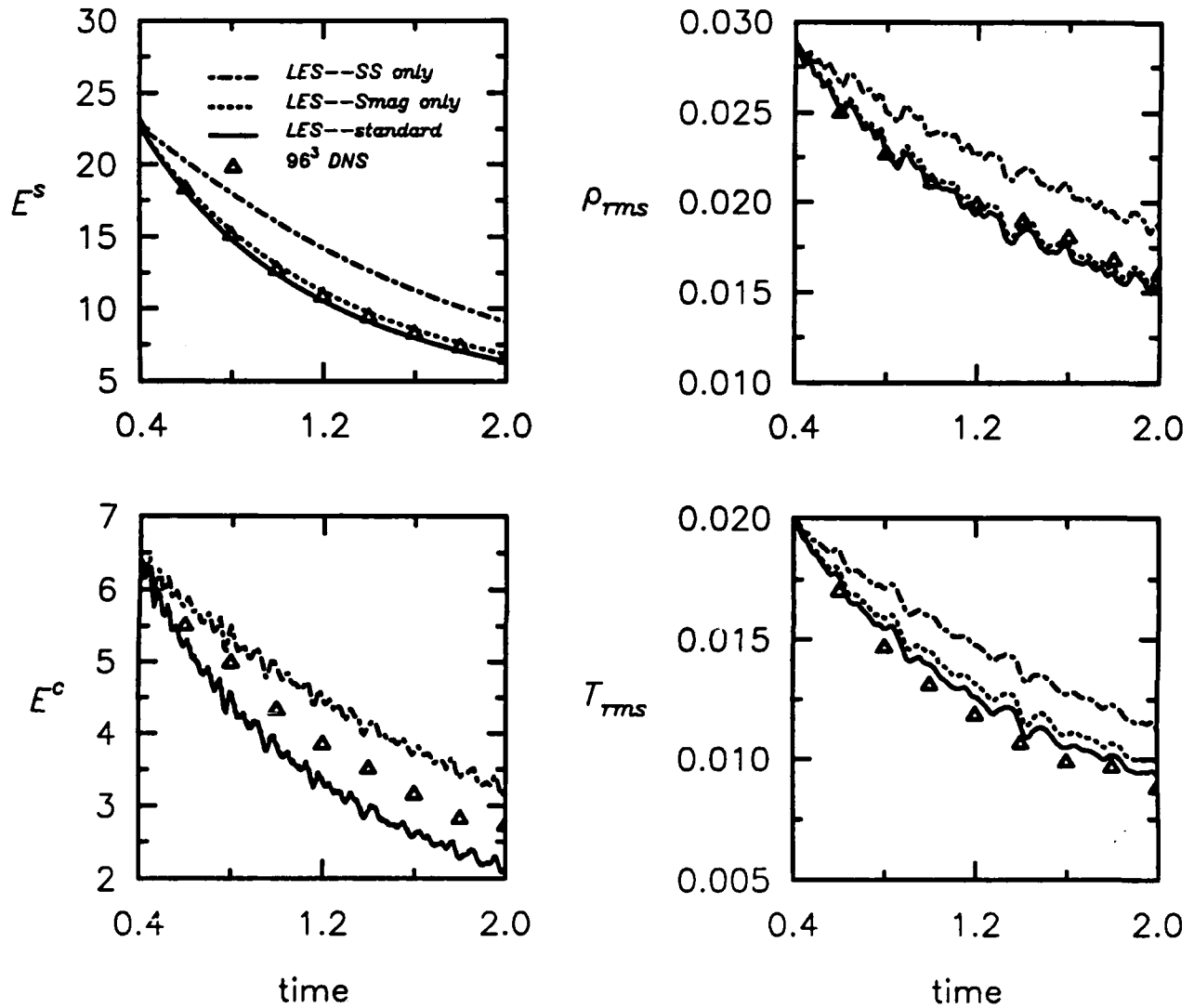


Fig. 19 — LES on a 32^3 grid of the case M01C02 using the *SEZHu* model with its recommended constants (case M01C02a). The results are compared with a well-resolved, 96^3 DNS. Also shown are the results for LES in which only the scale-similarity portion and only the Smagorinsky portion are employed

$M=0.1 \quad \chi=0.4$

standard model

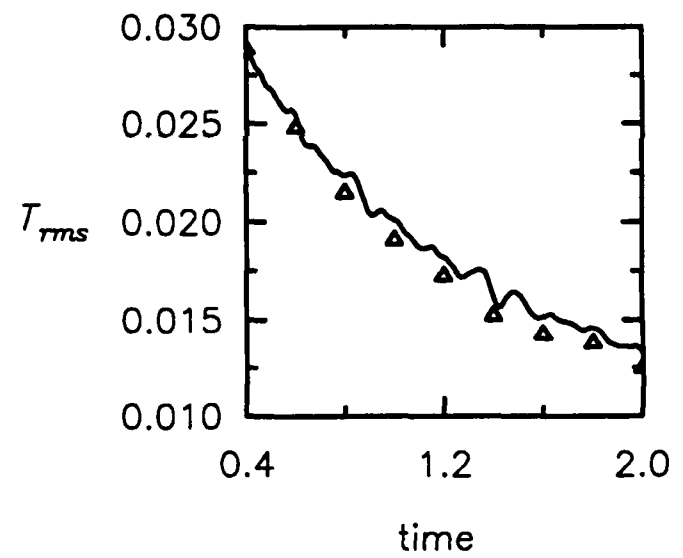
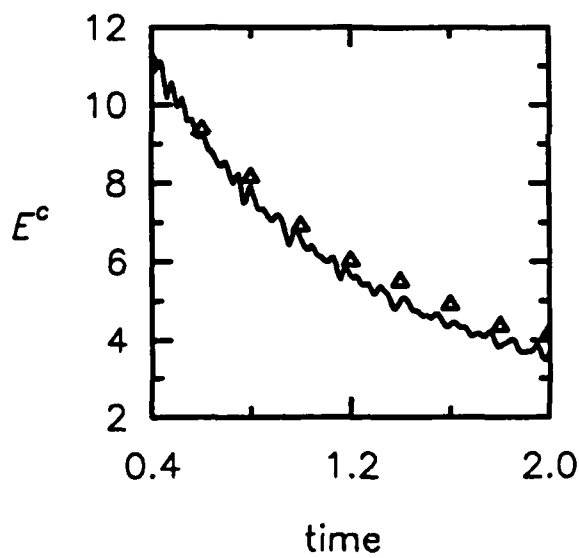
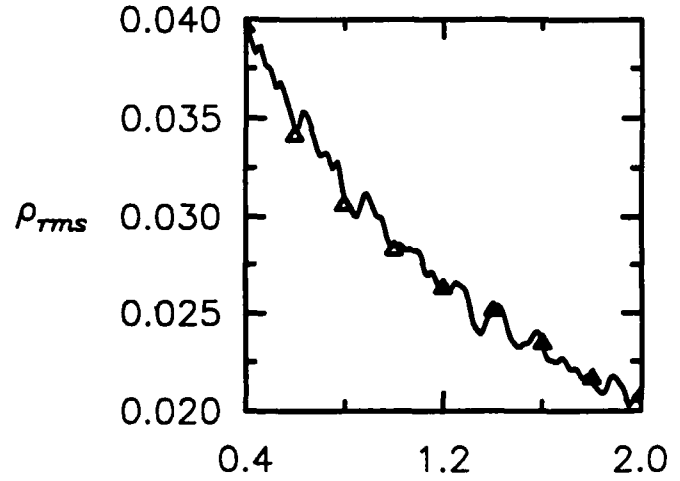
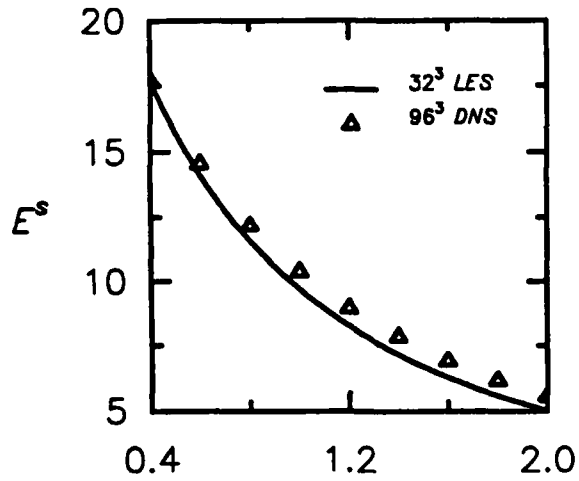


Fig. 20 — LES on a 32^3 grid of the case M01C04 using the *SEZHu* model with its recommended constants. The results are compared with a well-resolved, 96^3 DNS.

$M=0.1$ $\chi=0.6$

100% C_R 100% C_I 100% C_T

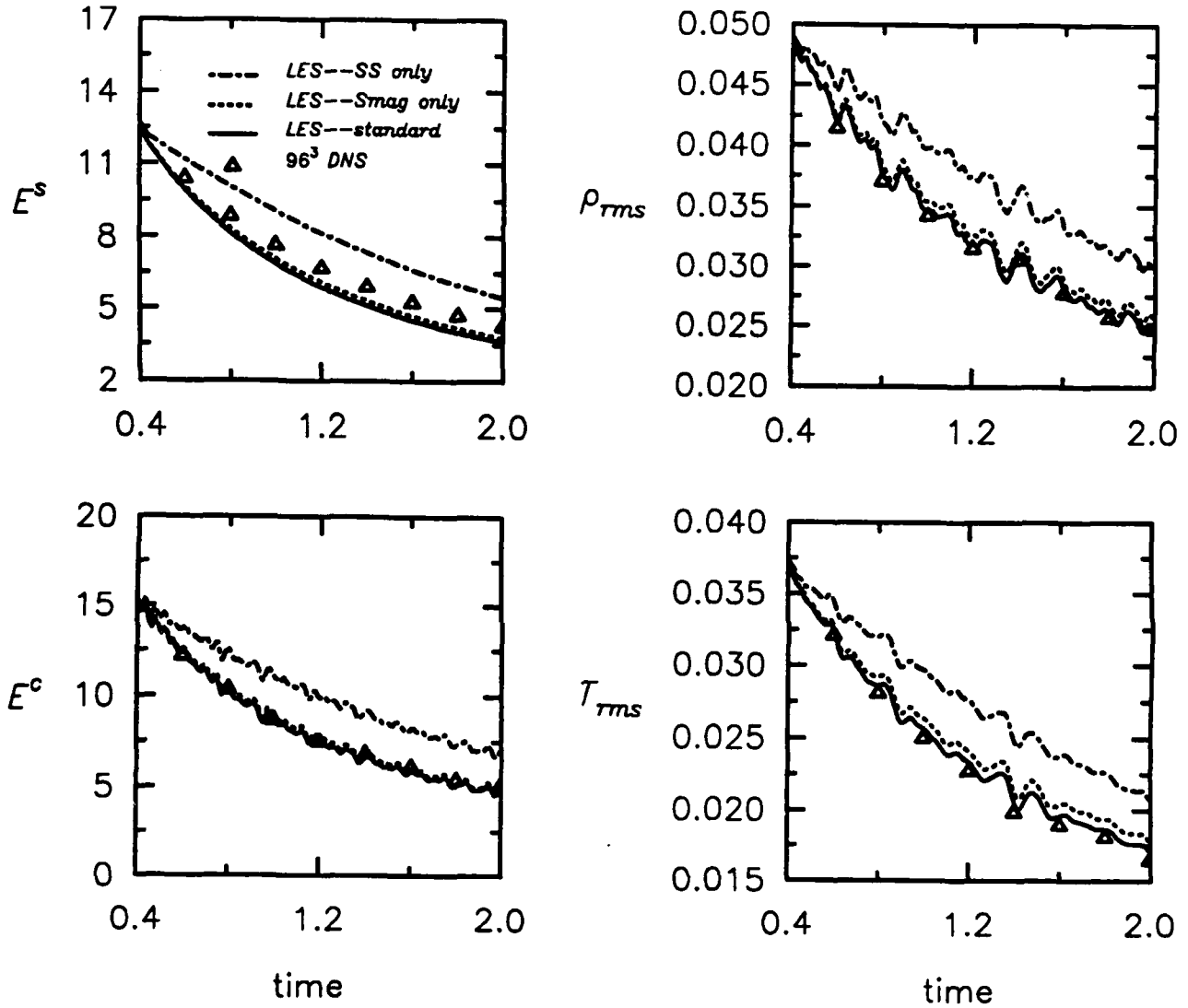


Fig. 21 — LES on a 32^3 grid of the case M01C06 using the *SEZHu* model with its recommended constants. The results are compared with a well-resolved, 96^3 DNS. Also shown are the results for LES in which only the scale-similarity portion and only the Smagorinsky portion are employed.

$M=0.2$ $\chi=0.2$

standard model

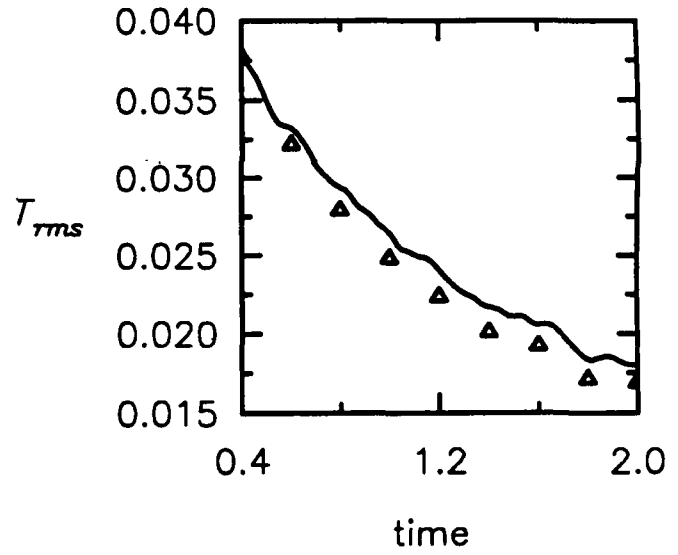
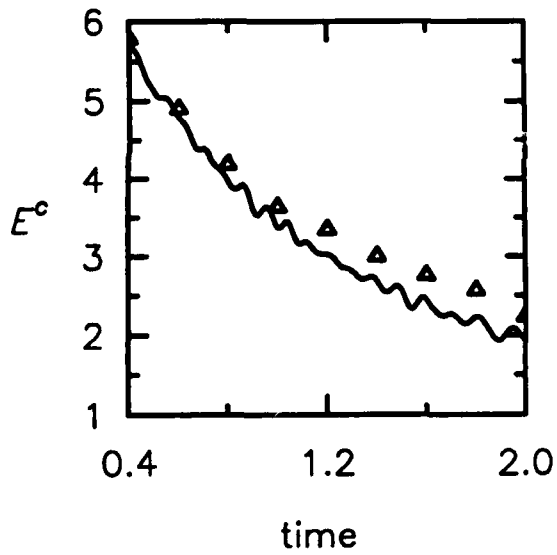
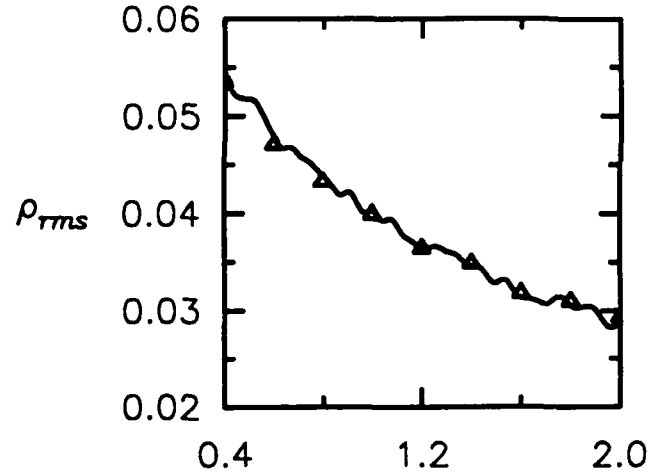
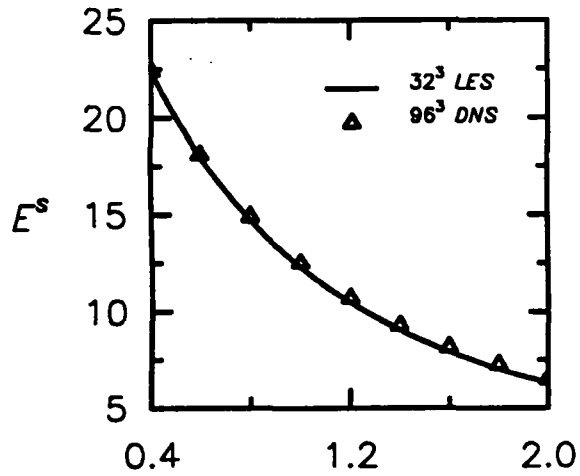


Fig. 22 — LES on a 32^3 grid of the case M02C02 using the *SEZHu* model with its recommended constants. The results are compared with a well-resolved, 96^3 DNS.

$M=0.3 \quad \chi=0.2$

standard model

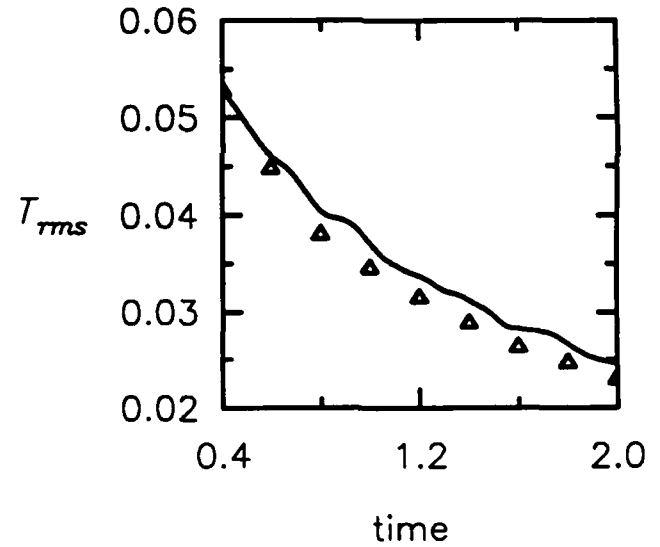
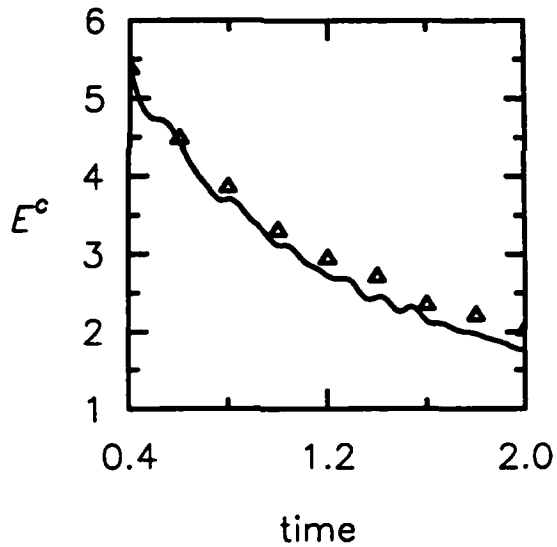
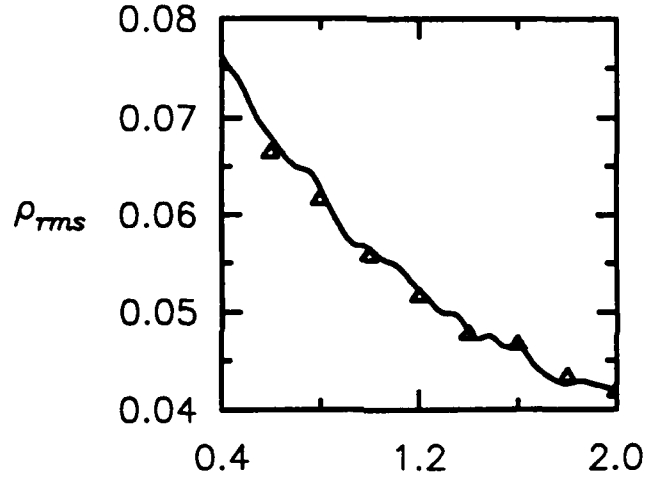
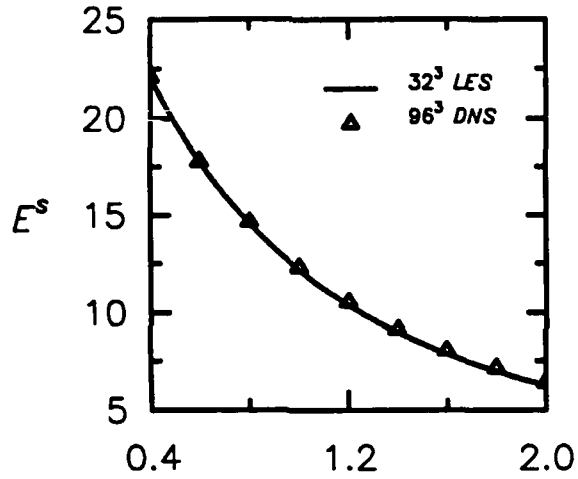
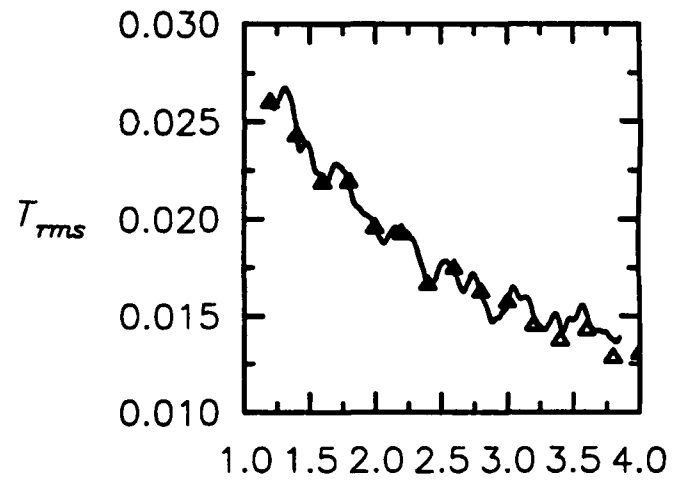
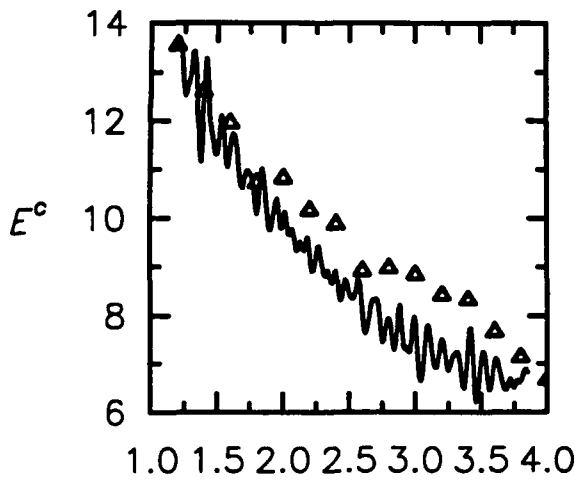
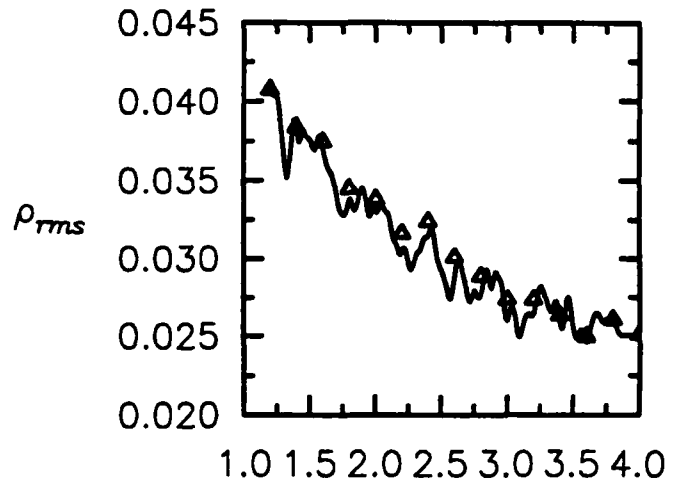
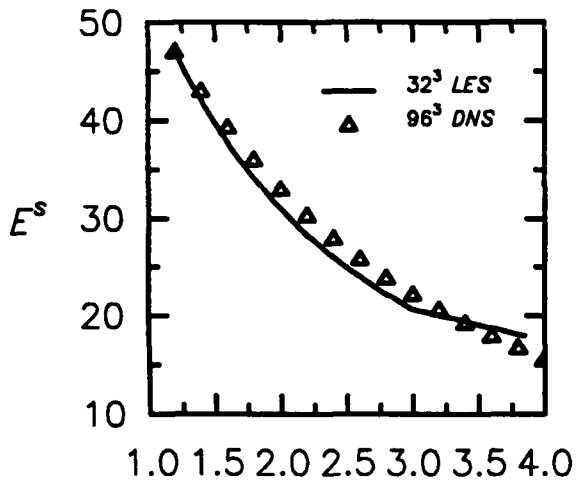


Fig. 23 — LES on a 32^3 grid of the case M03C02 using the *SEZHu* model with its recommended constants. The results are compared with a well-resolved, 96^3 DNS.

$M=0.1 \quad \chi=0.2$
 $k_0=5 \quad Re=250$

standard model



time

time

Fig. 24 — LES on a 32^3 grid of the case M01C02K5 using the *SEZHu* model with its recommended constants. The results are compared with a well-resolved, 96^3 DNS

$M=0.1 \quad \chi=0.2$

variation of C_R

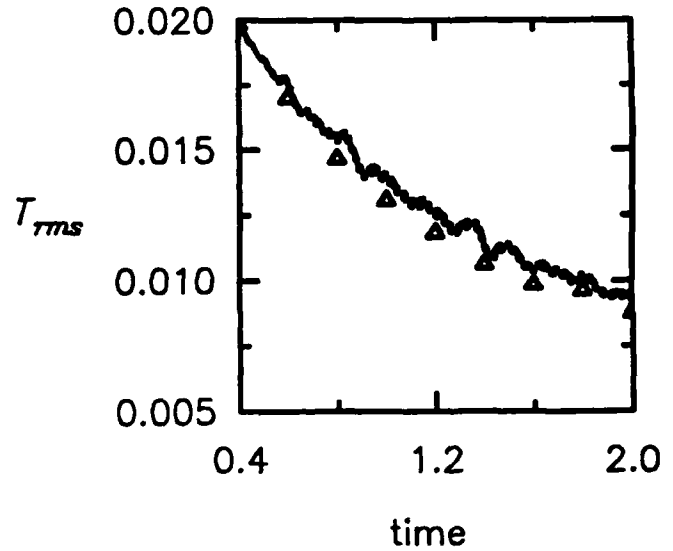
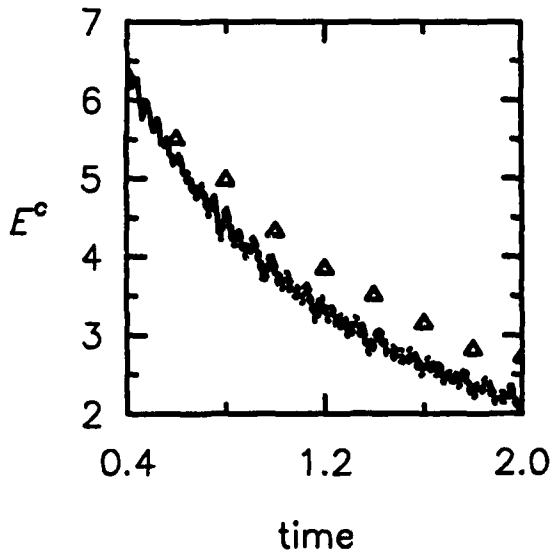
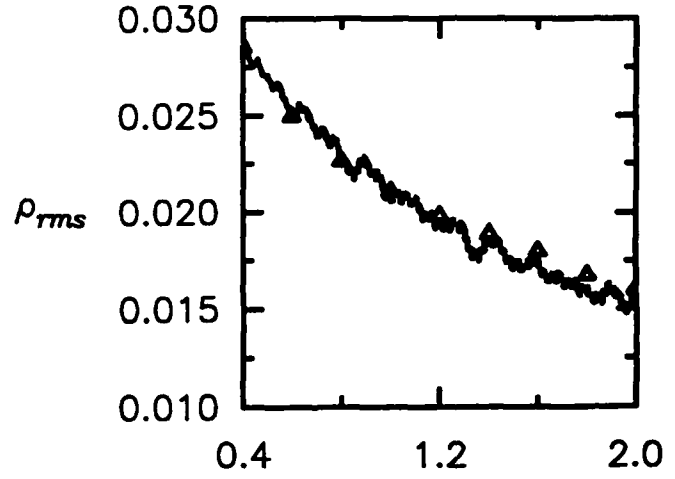
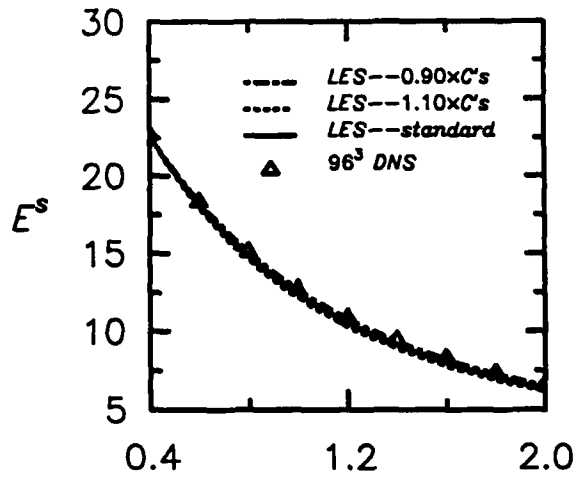


Fig. 25 — LES on a 32^3 grid of the case M01C02 using the *SEZHu* model with its recommended values of C_R and C_I and C_T (case M01C02a), with values 10% higher (case M01C02d), and with values 10% lower (case M01C02e). The results are compared with a well-resolved, 96^3 DNS.

$M=0.1 \quad \chi=0.2$

variation of C_I

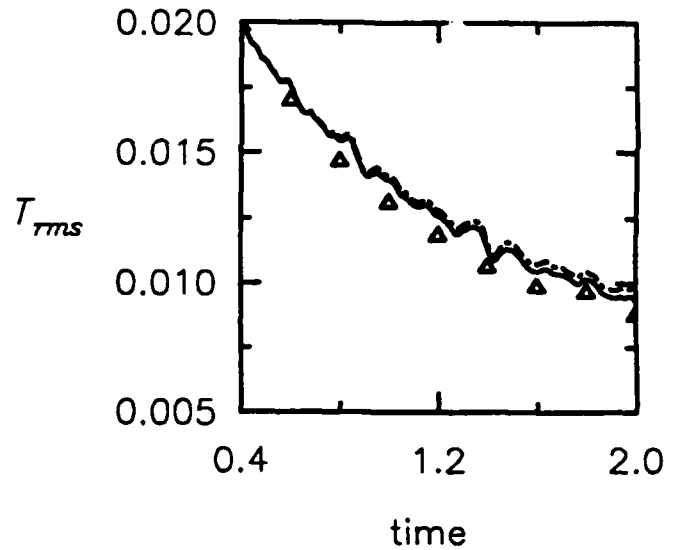
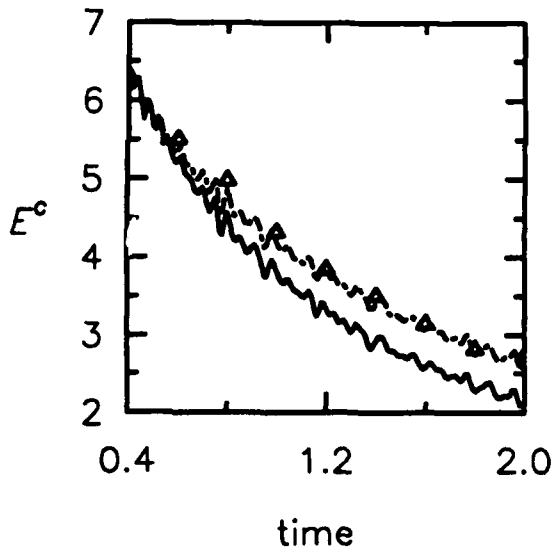
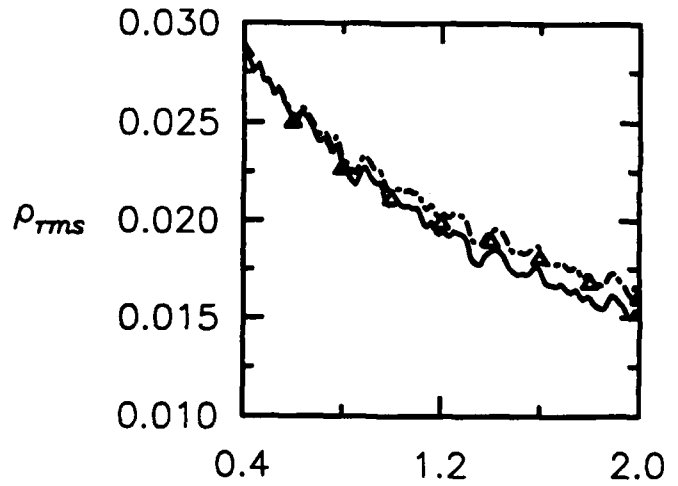
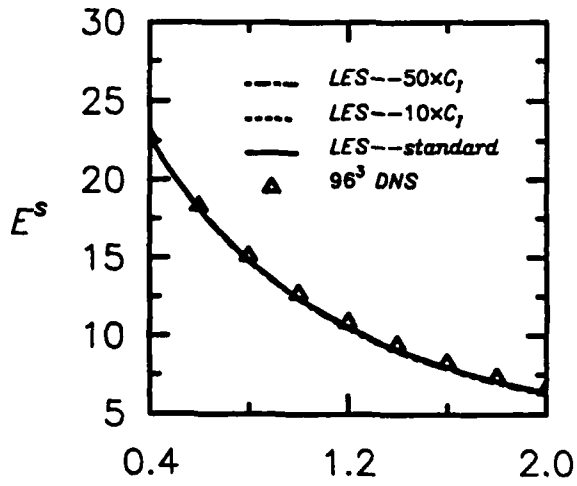


Fig. 26 — LES on a 32³ grid of the case M01C02 using the *SEZHu* model with its recommended values of C_R and C_T , but with $C_I = .0066$ (case M01C02a), with $C_I = .066$ (case M01C02m), and with $C_I = .330$ (case M01C02n). The results are compared with a well-resolved, 96³ DNS.

$M=0.1 \quad \chi=0.2$

variation of C_T

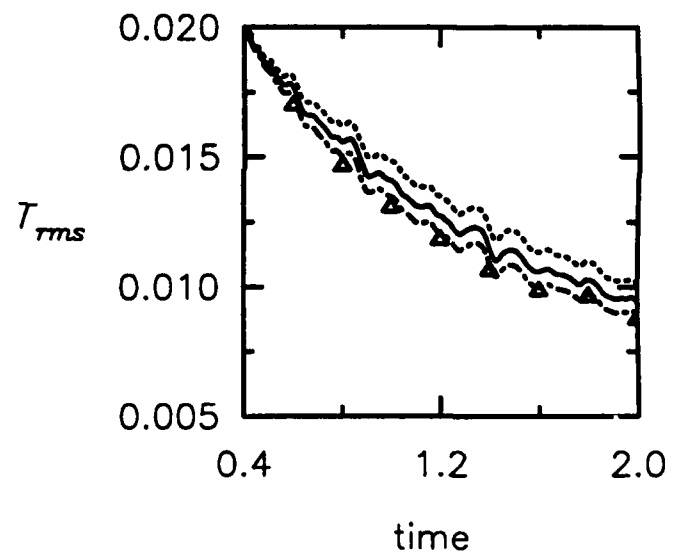
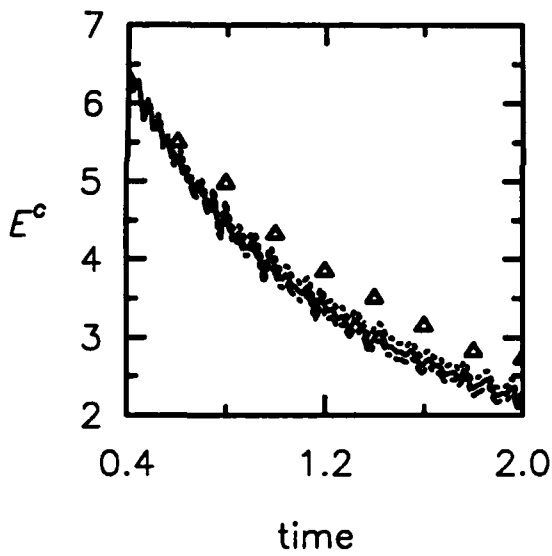
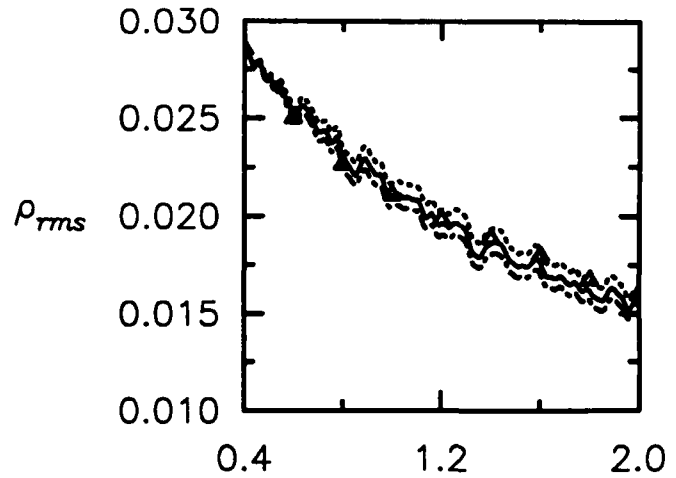
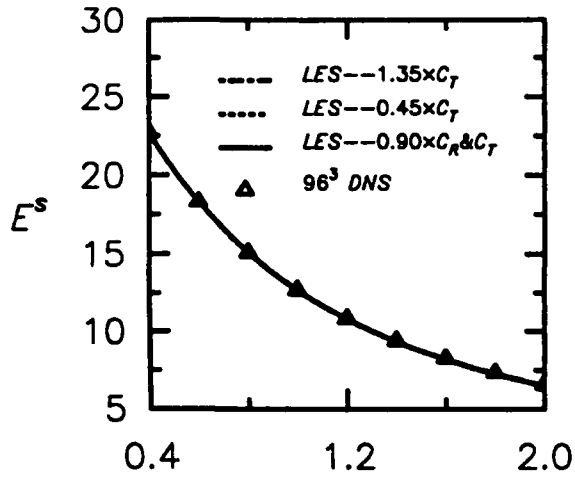


Fig. 27 — LES on a 32^3 grid of the case M01C02 using the *SEZHu* model with $C_R = 0.0108$ and $C_I = 0.0066$, but with $C_T = .0154$ (case M01C02g), with $C_T = .077$ (case M01C02j), and with $C_T = .0231$ (case M01C02k). The results are compared with a well-resolved, 96^3 DNS.

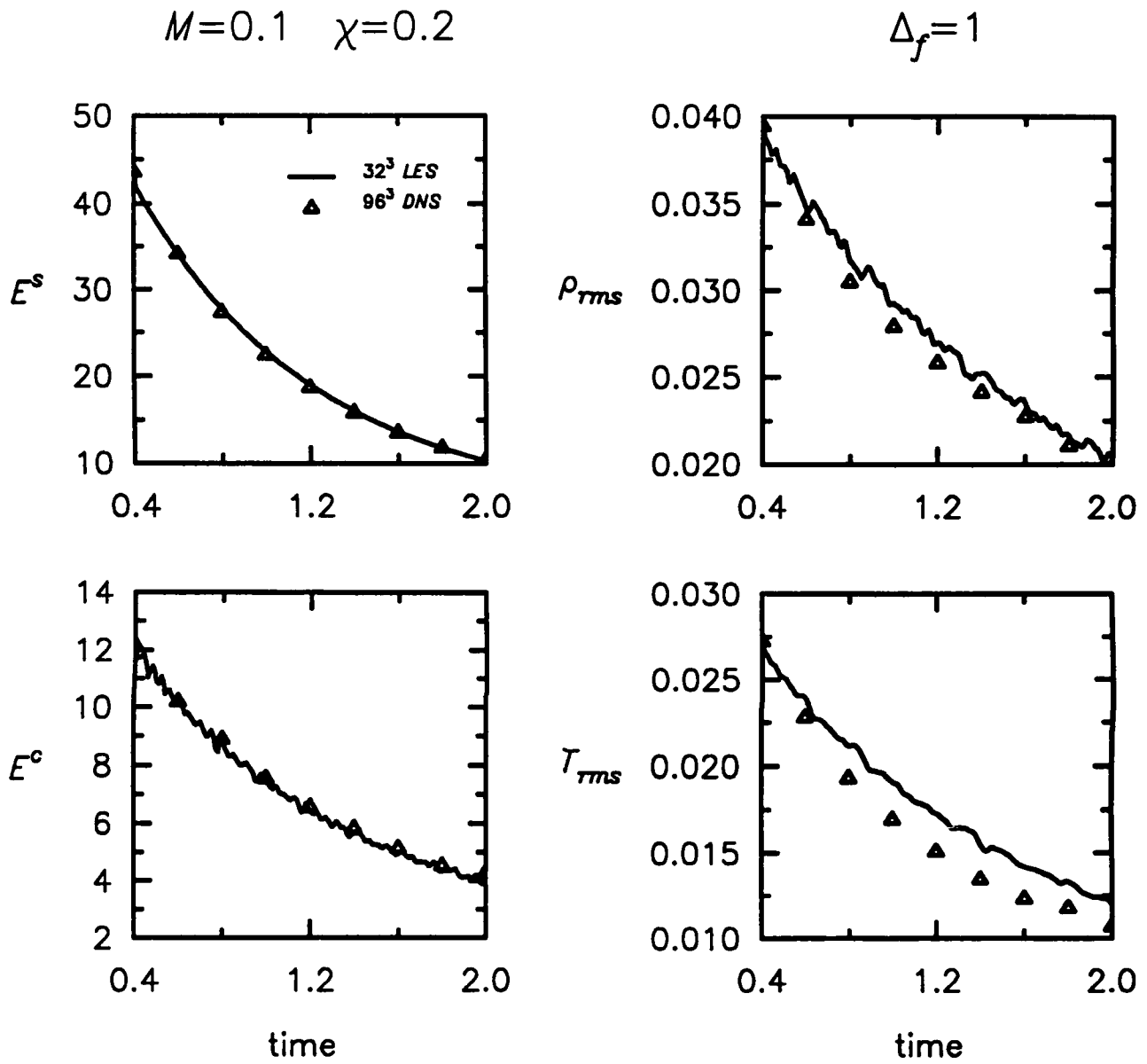


Fig. 28 — LES on a 32^3 grid, but with $\Delta_f = 1$, of the case M01C02 using the *SEZHu* model with its recommended constants (case M01C02h). The results are compared with a well-resolved, 96^3 DNS.

$M=0.1$ $\chi=0.2$

$\Delta_f=4$

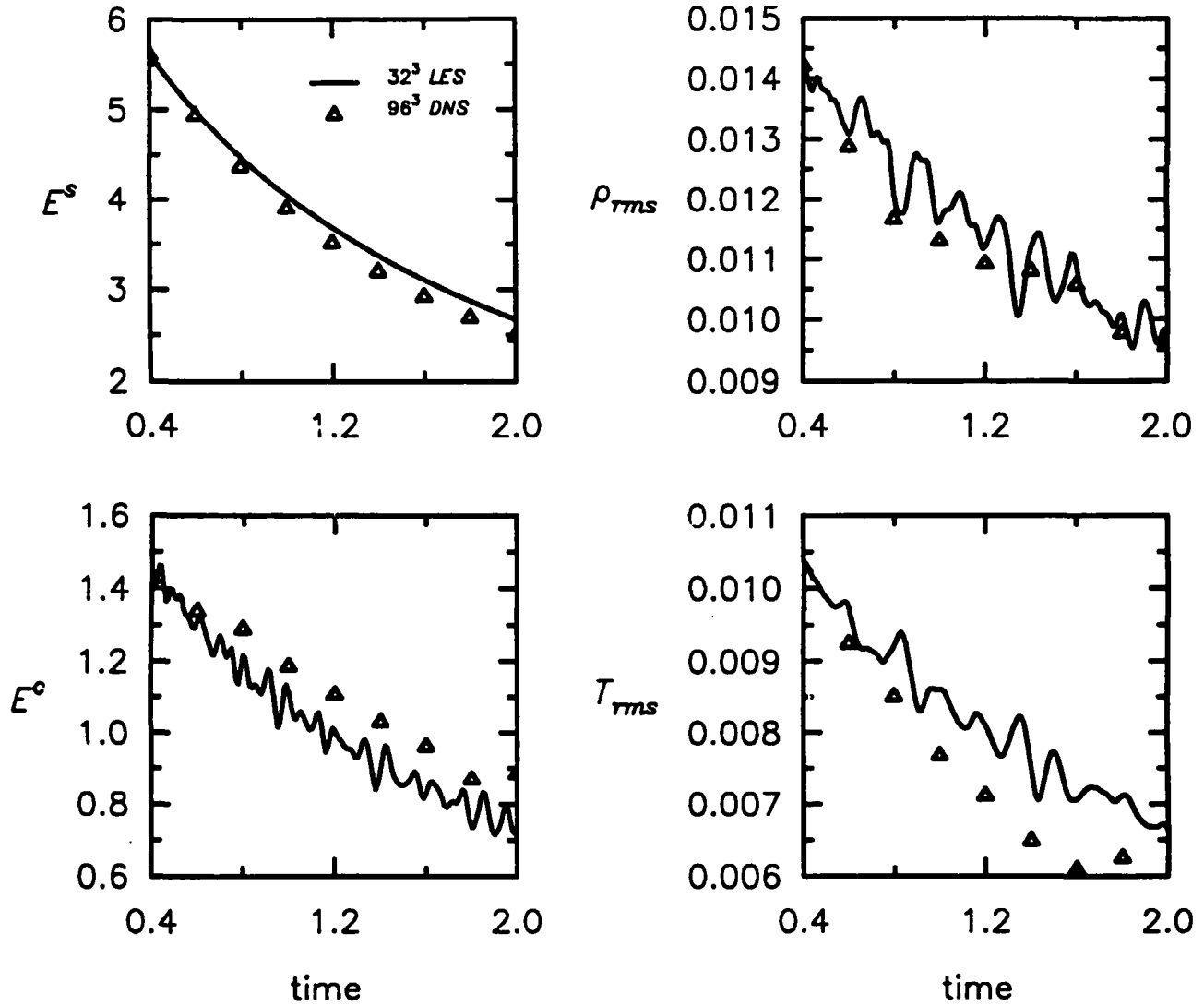


Fig. 29 — LES on a 32^3 grid, but with $\Delta_f = 4$, of the case M01C02 using the *SEZHu* model with its recommended constants (case M01C02i). The results are compared with a well-resolved, 96^3 DNS.

$M=0.1$ $\chi=0.2$

standard vs. revised

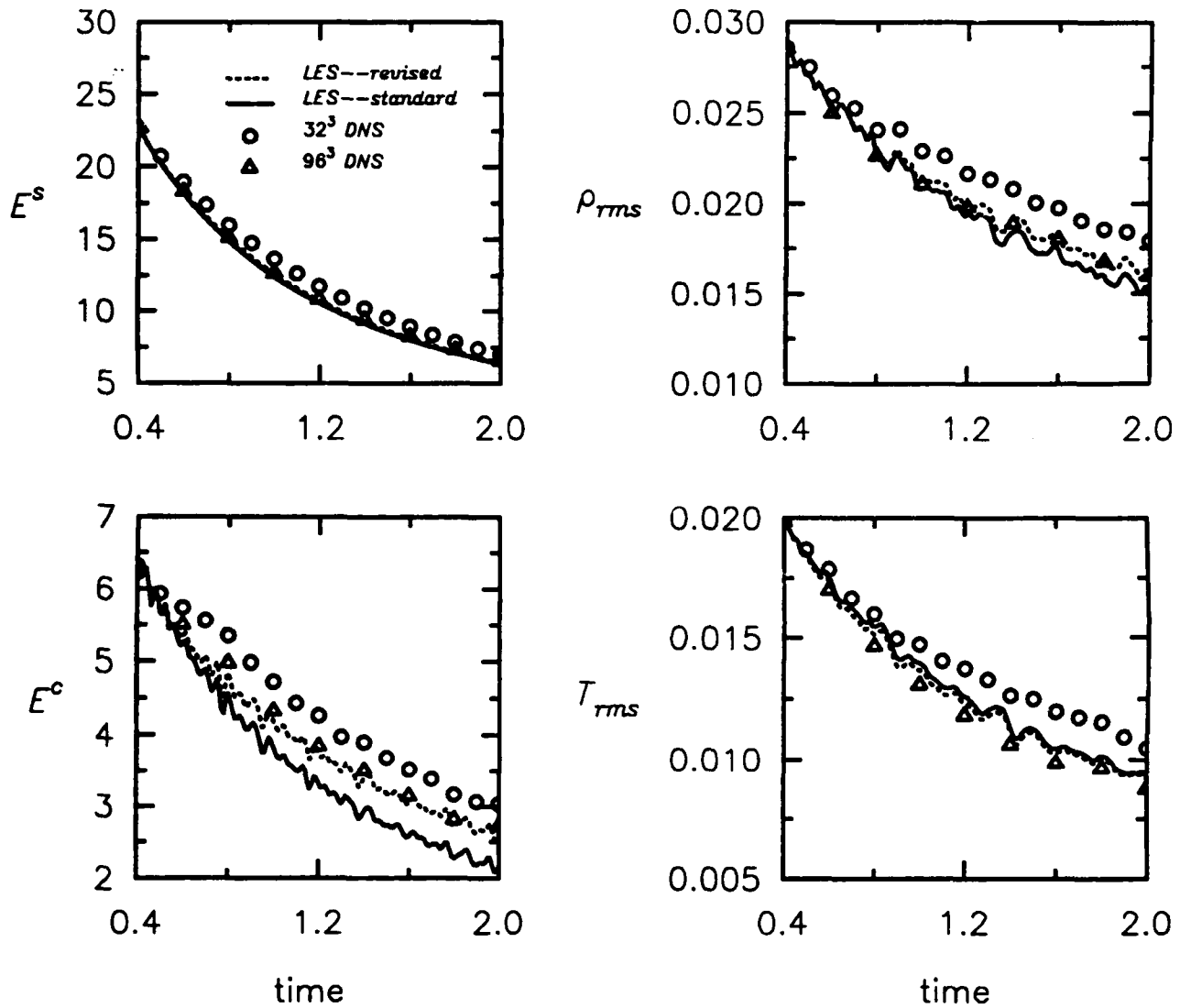


Fig. 30 — LES on a 32^3 grid of the case M01C02 using the *SEZHu* model with its revised constants and with its recommended constants. The results are compared with a well-resolved, 96^3 DNS and with a poorly resolved 32^3 DNS.

$M=0.1 \quad \chi=0.6$

standard vs. revised

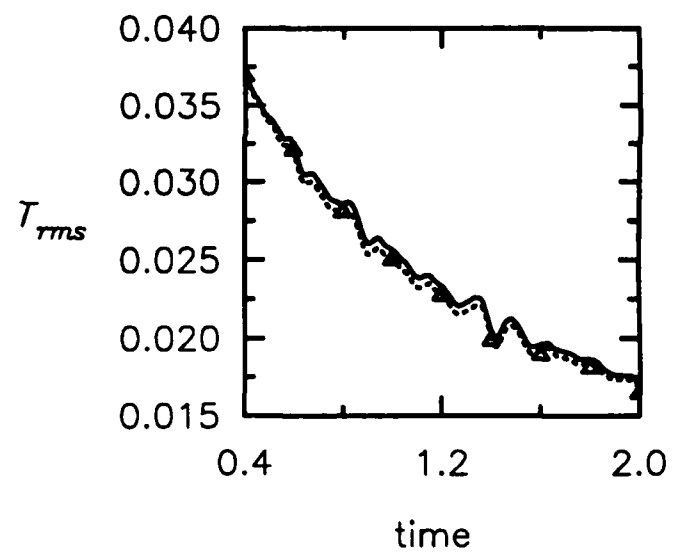
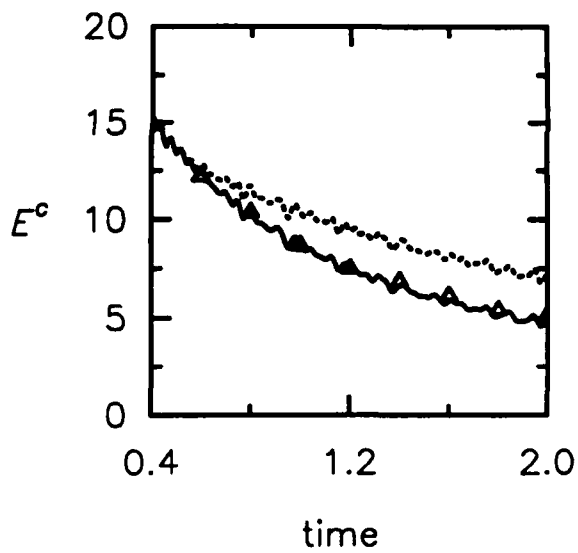
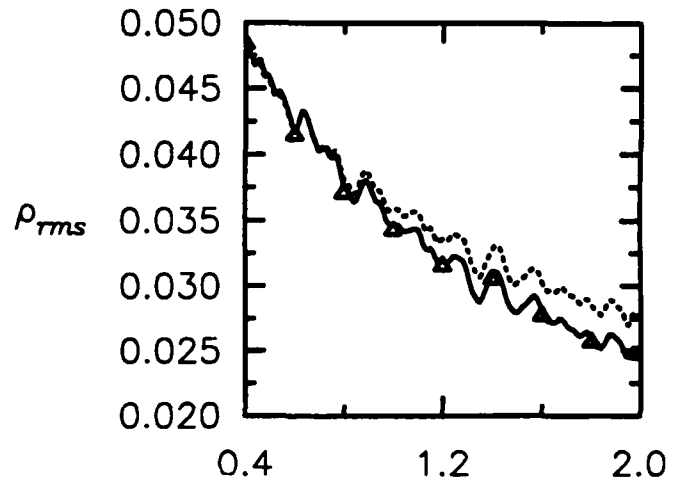
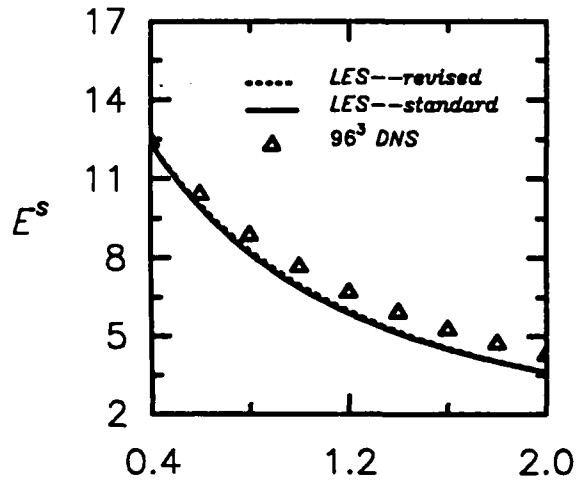


Fig. 31 — LES on a 32^3 grid of the case M01C06 using the *SEZHu* model with its revised constants and with its recommended constants. The results are compared with a well-resolved, 96^3 DNS.

$M=0.3 \quad \chi=0.2$

standard vs. revised

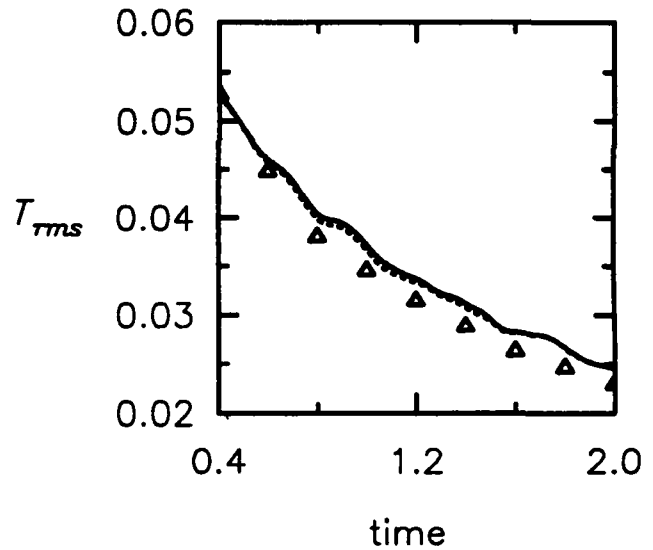
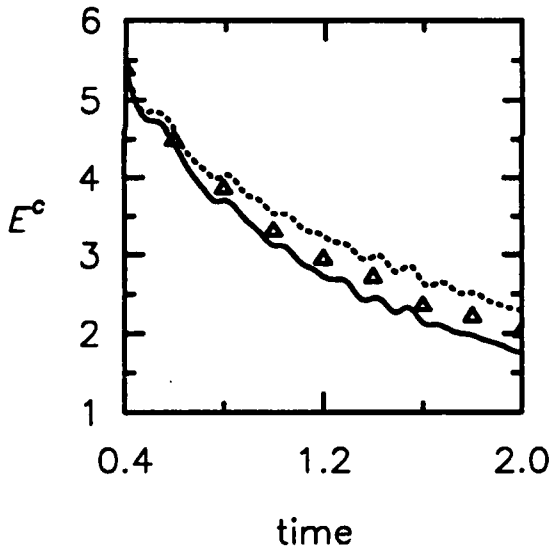
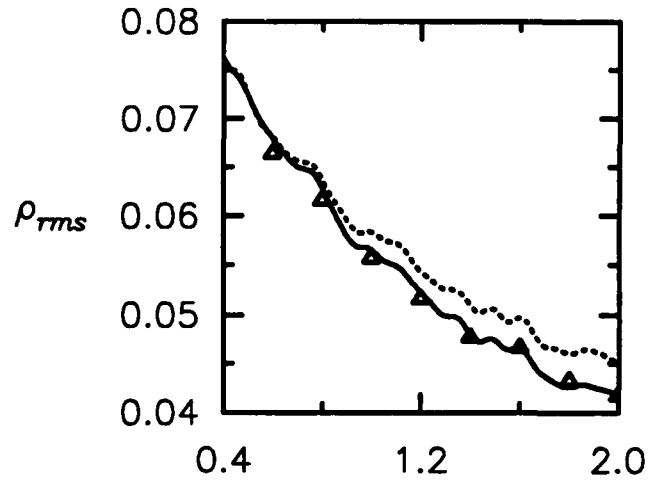
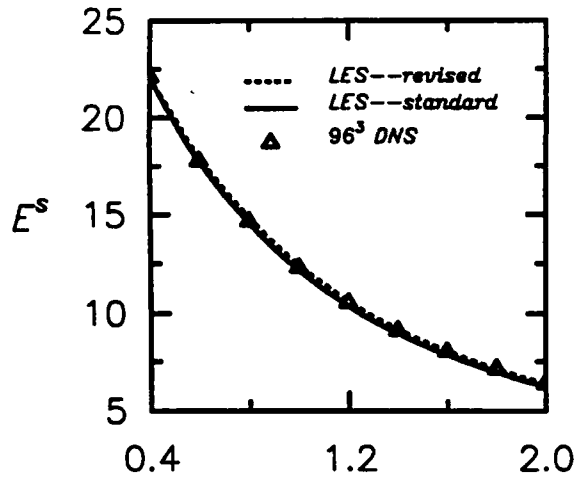


Fig. 32 — LES on a 32^3 grid of the case M03C02 using the *SEZHu* model with its revised constants and with its recommended constants. The results are compared with a well-resolved, 96^3 DNS.